Fabrication and Characterization of Materials for Ultrafast Electron Scattering Experiments

Syed Ali Hassan

Department of Physics
McGill University, Montreal
December 2023

A thesis submitted to McGill University in partial fulfillment of the requirements of the degree of Master of Science

Abstract

Ultrafast Electron Scattering (UES) as a technique has unique capabilities in terms of interrogating the fundamental processes that underly the novel properties of 2D-layered and strongly-correlated materials with subpicosecond temporal resolution. Despite its potential to deliver important new insights into such materials, the implementation is hampered by an intricate issue of its specific sample requirements. The sample must be macroscopic in lateral dimensions ($\sim$100 microns) and thin ($\sim$10s of nm) enough to allow electrons to penetrate and interact with the material's structure. In this thesis, a novel approach is adopted, modified, and implemented to achieve high-quality throughput samples for UES experiments. This approach involves exfoliating layered materials via metal Gold(Au)-assisted tape. This method prove particularly effective on materials like WS_2, SnS_2, Graphite and high-temperature superconductor Bi-2212 ($Bi_2Sr_2CaCu_2O_{8+x}$), which resulted in producing laterally extended ($\geqslant 200\mu$m), and ultra-thin (< 5 nm) single crystals flakes. In addition, Transmission Electron Microscopy(TEM), Raman spectroscopy, and UES techniques were used to qualitatively characterize the nature of these materials.

Intrinsically 3D materials can also be prepared for UES experiments via thin film deposition approaches. Previously, the Siwick group had investigated VO_2 films prepared by PLD (Pulsed Laser Deposition) technique. However, this time we encountered many notable problems with PLD grown VO_2 thin film samples. To address those issues, we systematically investigated the quality and phase of VO_2 thin films. Our diagnostics reported the presence of an unusual B-phase, which did not align with our inclination to research on VO_2 M1-phase in UES trials. After adjusting the PLD parameters, we received a fresh batch of VO_2 samples that displayed the desired M1 to

R (rutile) Phase transition on $\sim 56^oC$. Upon addressing the concerns, we are prepared to start the novel Debye-Waller experiments soon.

Abrégé

La Diffraction Ultrarapide par Électrons (DUE) possède des capacités uniques permettant d'explorer, avec une résolution temporelle inférieure à une picoseconde, les processus fondamentaux qui sous-tendent les nouvelles propriétés des matériaux 2D et systèmes fortement corrélés. Cependant, malgré son potentiel à révéler ces nouvelles propriétés, la mise en œuvre de cette technique est entravée par les strictes restrictions imposées aux échantillons utilisés durant les expériences. En effet, l'échantillon doit être macroscopique en dimensions latérales ($\sim$100 micromètres) et suffisamment mince ($\sim$10 nanomètres) pour permettre aux électrons de pénétrer l'échantillon et d'interagir avec la structure interne du matériau.

Dans cette thèse, une nouvelle approche est adoptée et mise en œuvre pour obtenir des échantillons de haute qualité conçus pour les expériences de DUE. Cette approche consiste à exfolier des matériaux en couches via une bande adhésive assistée par un métal d'or. Cette méthode s'avère particulièrement efficace sur des matériaux comme le Disulfure de Tungstène (WS_2), le Sulfure d'Étain (II) (SnS_2), le Graphite et le supraconducteur haute température Bi-2212 ($Bi_2Sr_2CaCu_2O_{8+x}$). Cette approche a permis la production de flocons monocristaux d'une longueur supérieure à ($\geqslant$ 200μm) et d'une minceur inferieure à (< 5 nm). De plus, les techniques de Microscopie Électronique en Transmission (MET), spectroscopie Raman et UES ont été utilisées pour qualitativement caractériser la nature de ces matériaux.

Les matériaux intrinsèquement 3D peuvent également être préparés pour les expériences de DUE via une approche de dépôt de couches minces. Auparavant, le groupe Siwick avait étudié des films d'Oxyde de vanadium (IV) (VO_2) préparés par la méthode d'ablation laser pulsé (PLD), cependant, de nombreux problèmes ont été rencontrés. Pour résoudre ces problèmes, nous avons

systématiquement étudié la qualité et la phase des films minces de VO_2. Nos diagnostics ont signalé la présence d'une phase B inhabituelle, ce qui ne correspondait pas à notre penchant d'étudier la phase M1 de VO_2 dans des expériences de DUE. Après avoir ajusté les paramètres de PLD, nous avons reçu un nouveau lot d'échantillons VO_2 qui affichaient la transition de phase souhaitée à $\sim 56^o$C (de phase M1 à phase rutile (R)). Après avoir résolu d'autres problèmes dans notre laboratoire, nous sommes prêts à lancer de nouvelles expériences de Debye-Waller.

Acknowledgements

As I pause on this significant threshold of my journey to reflect on the myriad of individuals who have enriched my path, my heart is filled with profound gratitude. To Dr. Bradley J. Siwick, a guiding light in the world of science and an unwavering pillar of support throughout my MSc. At McGill thankyou for entrusting me with the freedom to explore and for steering me towards a horizon of understanding that has become the bedrock of my scholarly quest.

To my comrades in research, Tristan Britt, Laurent René de Cotret, Martin Otto, Sebastian Hammer, Malik Lahlou, Laurenz Kremeyer, and to every soul in the Kambhampati research team, your camaraderie and insightful feedback have been indispensable. The environment we've cultivated together has been one of mutual growth and relentless pursuit of excellence. A salute to Pascal Brourseguin and Robert Gagnon the technicians whose skills have been the invisible yet crucial framework of our collective endeavor. Your dedication forms the backbone of discovery, and for that, I am truly thankful.

I am also grateful to my friends and colleagues within the physics department, with whom I've shared both professional milestones and moments of leisure. Professors David Cooke and Peter Grutter, your guidance has been instrumental in where our scholarly journeys intersected.

To Hadia e Fatima, my anchor, and my family, whose love is as deep as the ocean and as constant as the tides. Your belief in me has been the quiet force that thrived me forward. Finally, I am grateful for the love and support of my parents Syed Ali Naseem Kazmi and Asmat Tahira Kamzi, who inspired me to reach my full potential.

To my Parents and beautiful Wife.

Table of Contents

List of Figures

Chapter 1

Introduction

Our perception regarding the structural and compositional phase of condensed materials is often built on the underlying ideas behind electronic structure and the atomic lattice at thermodynamic equilibrium. Recent research has focused on the longsighted dream of visualizing the complex lattice dynamic evolution in materials in "real-time", with the highest spatial resolution. In order to control and manipulate complex materials out of equilibrium, new methodologies must be created that can follow dynamical processes in materials with extremely fine spatiotemporal resolution. Ultrafast electron scattering (UES) is one such technique. In the following chapter, we describe this technique, its goals, and the observables that can help researchers to develop a deep understanding of complex structural responses in real-time.

1.1 Inspiration and Goals

A first-principles understanding of a material's qualities and behavior requires an in-depth knowledge of its atomic to microstructure. Numerous scientific and engineering applications use this knowledge as a foundation of several applications. Transmission Electron Microscopes (TEMs) are one of the techniques that play a pivotal role in gathering important data about the structures of materials. It provides a special ability to study materials at the atomic and nanoscale levels. It can directly image and analyze the interior structure of thin materials by penetrating through them with a concentrated electron beam. With the suite of techniques available in a modern TEM instrument, researchers can understand the arrangement of atoms, crystal defects, grain boundaries, and other microstructural properties. But materials are not static; they undergo dynamic processes that significantly influence their properties; thus, when it comes to studying dynamic structural changes, conventional TEMs are extremely limited to their abilities.

One solution to overcome this issue is through ultrafast spectroscopic techniques. The emergence of femtosecond lasers has revolutionized the study of ultrafast processes in materials. These lasers emit ultra-short light pulses with durations on the order of a few femtoseconds. The timescales of many fundamental processes that take place in materials are in accordance with this ultrafast periods i.e., the lattice vibrations or phonons. The pump-probe spectroscopies have been implemented successfully to study a wide variety of phenomena, that includes chemical reactions in both the gas [6] and liquid phase [7], phase transitions in correlated materials [8], and the function of proteins [9]. To examine biological molecules, 2D IR spectroscopy has been employed extensively. The pulse sequences used are optical analogues to those used in nuclear magnetic resonance (NMR) spectroscopy [10]. Interestingly, the terahertz (THz) regime has also been included in the scope of ultrafast spectroscopy. These THz pulses can be obtained using many types of approaches, allowing us to examine the ultrafast dynamics of low energy (meV) processes [11]. Similarly, Angle-resolved photoemission spectroscopy (ARPES), provides the facility to visualize the electronic correlation in reciprocal (k) space [12]. Time-resolved Raman (TRR) spectroscopy can detect lattice excitations, but it's limited to phonons with nearly zero momentum [13]. Although several types of ultrafast spectroscopies have provided a plethora of information, but they still haven't been able to reveal direct structural information.

An alternative and nuanced approach to tackle the aforementioned problem involves combining ultrafast lasers with TEMs. For example, techniques such as stroboscopic or using laser pulses alone have allowed the direct observation of ultrafast dynamical processes. A femtosecond laser pulse (pump) is used to excite the material, initiating a structural change, while a delayed probe pulse captures the subsequent structural evolution [1]. A famous stroboscopic technique called Ultrafast electron scattering (UES) has the capability to entangle aforementioned anomalies. In this pump-probe technique, the subject material is perturbed with ultrashort (pump) laser pulses by precisely controlling the time delay $\Delta\tau$, a beam of electron pulses (probe) scatters from the material's lattice forming a scattering pattern in reciprocal space. The main objective of this introductory chapter is to present the basic, theoretical, and experimental descriptions of this principal technique used in our current and future experiments.

1.2 Experimental Technique

1.2.1 Introduction to Ultrafast Electron Scattering (UES)

UES combines the tools and techniques of ultrafast laser spectroscopy with those of TEM to enable the real-time investigation of structural dynamics in materials. By synchronizing a pulsed electron beam with femtosecond laser pulses and repeating measurements for many delays, this technique can record diffraction patterns and provide instantaneous evolution of the atomic configuration within materials. In order to achieve this, UES system relies on the integration and synchronization of other individual components. In addition to providing a brief overview of the theory of electron diffraction, this chapter will describe the construction, settings, and use of our table-top diffractometer.

A schematic overview of our experimental setup used throughout this thesis is shown in Figure 1.1. In general, the technique uses femtosecond laser pulses for both pump and probe, splitting them with a beamsplitter. The path of the pump pulse can be adjusted to vary its length, allowing for manipulation of the pump-probe delay. The electron (probe) pulses are generated by considering the Photoelectric effect. The electron probe pulses produced are propelled by electromagnetic fields and guided through magnetic solenoid lenses, passing through a Radio Frequency (RF) compression cavity, interacting with the sample, and eventually reaching an ultrafast CCD camera. The subsequent sections will provide a thorough description of the configuration and optimization process specifically tailored for UES.

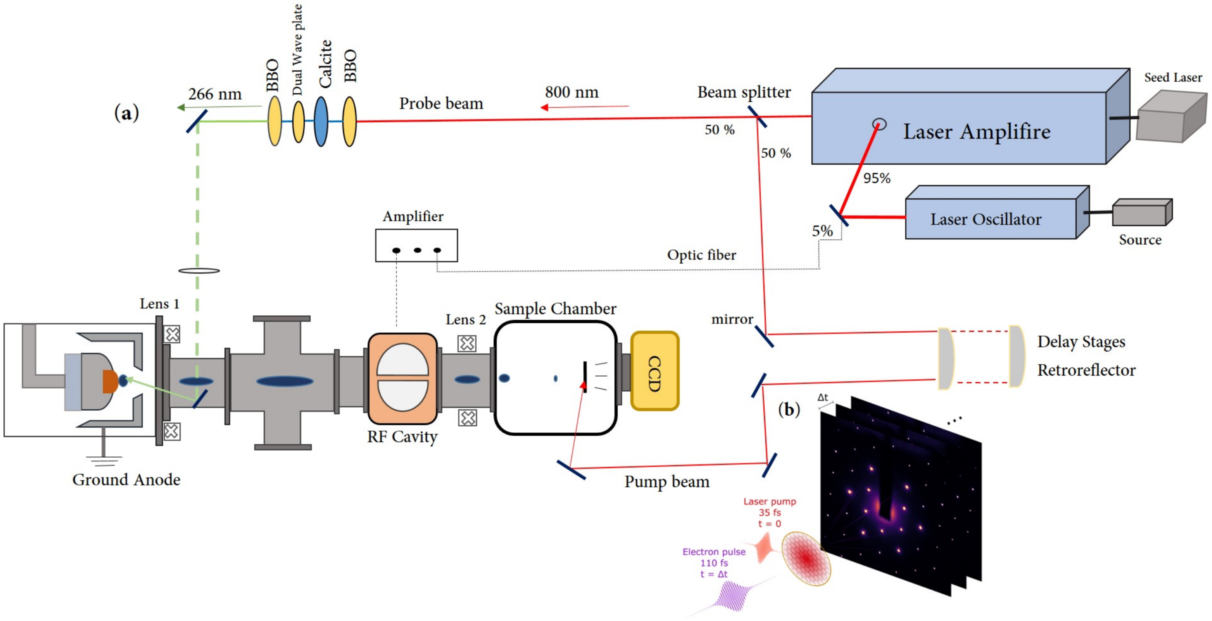

Figure 1.1: (a) A schematic of our UES setup. A laser oscillator simultaneously powers a laser amplifier and engages a phase-lock loop. Laser from the amplifier is splitted between a pump and a probe beam. The probe beam used to generate electron beam via Photoelectric effect, and the RF cavity functions as a temporal lens to concentrate the probe electron beam onto the sample, and CCD camera. (b) Pump-probe electron diffraction experiment simplified in a schematic. Ultrashort pump pulse excites the specimen and starts a physical process of interest at time t=t_0 (time-zero). The probe beam takes a picture at a specific time delay after excitation, $\Delta\tau$. The sample's atomic structure is encoded by the position and strength of the diffraction peaks.

1.2.1.1 Optical Arrangements of UES

The system starts with a mode-locked Titanium:Sapphire oscillator (Spectra-Physics), producing $\sim$35fs pulses at a repetition rate of approximately $\sim$75MHz. The central wavelength is 800nm, and the pulse energy is approximately $\sim$5nJ. A portion of the oscillator beam is divided, with 5% directed towards the RF system for synchronization and electron pulse compression, while 95% serves as the input seed laser for a regenerative Titanium: Sapphire laser amplifier (Spectra-physics Spitfire XP pro). The oscillator system is systematically synchronized with a laser amplifier which takes $\sim$75 MHz at input and amplifies it to a 1 kHz signal. This 1 kHz signal sets off a group of Pockels cells, which choose a laser pulse to be amplified and permit it to spend a particular amount of time ($\sim$100 ns) in the cavity for the best possible amplification. These amplified pulses are then ejected from the cavity, re-compressed, and the output energy is obtained nearly above 3 mJ/pulse. We also notice from the experimental schematic that the amplified beam is split into two 50%/50% on the optical table, where one is for the pump and the other for probe beams, respectively. The pump beam is used for Photo-excitation of the targeted samples, which passes through a variable retro-reflector delay stage, that controls the time delay between pump and probe pulses. The probe electon beam is a frequency tripled using a non-linear optical process called third harmonic generation. This is done by sending the beam through an organized sequence of three crystals, BBO (beta-barium borate), calcite, and BBO, in a specific arrangement [14]. Frequency tripling is the process where 800nm and 400nm wavelength of the laser is removed, and the remaining ultraviolet light $\sim$267nm is obtained, which is later on focused and coupled into an ultrahigh vacuum beamline at the other end of the sample chamber. The ultraviolet (UV) light ($\sim$267 nm) reflects off an aluminum mirror and is aligned onto a copper DC photo-cathode which is at a voltage of -100 kV. we will discuss in-depth details in the next sections. The sample chamber and attached CCD camera are maintained to a high vacuum level ($\sim 10^{-7}$ Torr). During our recent upgrades of UES instrument, I designed and constructed a retractable Faraday cup to measure the electron beam current. Additionally, a new cryogenic arm (cold-finger) with temperature sensor installed, that has the capability to cooled down the samples as low as $\sim$10K.

1.2.1.2 Electron Gun

Figure 1.2 represents the schematic of the electron beamline. The electron source (photocathode) is held in a cylindrical vacuum chamber under $\sim 10^{-7}$ Torr pressure. High voltage feedthrough rated for 100kV enters through the top of the chamber which is connected to the highly stable voltage power supply (0.001% at 100kV). This level of stability provides an arrival time jitter of ≤ 10 fs for the cathode sample distance in compact geometry. For the generation of sub-picosecond electron pulses, a copper cathode is illuminated with a frequency-tripled UV pulse of ultraviolet (4.6 eV) light. We use Copper as it has a moderate work function, typically around 4.5 to 5.1 eV. The work function is the minimum energy needed to remove an electron from the surface of a metal. The

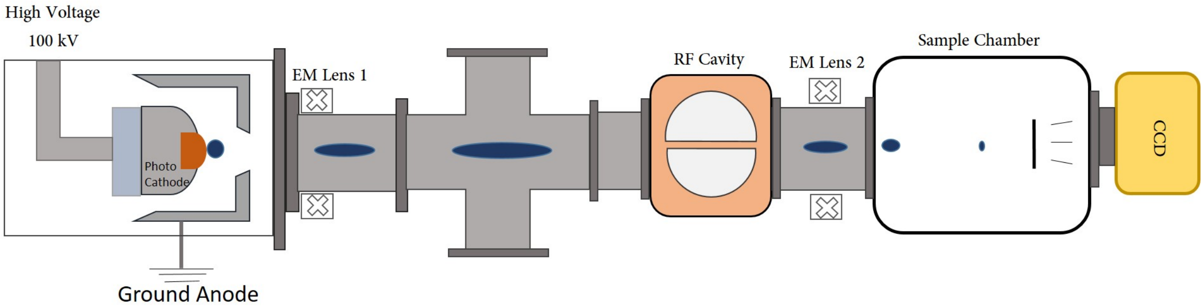

Figure 1.2: Schematic of the probe beamline, where the electron beam is accelerated at 100 kV after emission from the Cu cathode, travels through EM lens 1, the RF cavity for electron bunch compression, and is then steered and focused by EM lenses 2 onto the sample, which is located inside the sample chamber.

cathode is maintained at a voltage close to -100 kV relative to the grounded anode. Accordingly, an ultrashort cloud of photoemitted electrons is created by shining a light on a Cu cathode at or above its work function [15]. A solenoid lens collimates (transversely focused) the electron beam. Further down the beamline, the electron pulse undergoes longitudinal space-charge broadening.

The primary technical challenge to performing high-time resolution UES with high signal-to-noise is the space-charge expansion. The generated electron pulses have a high charge density, that mostly leads to Coulomb's repulsion, which initiates dispersive velocity broadening in both the longitudinal (propagation axis) and transverse (radial) directions in the rest frames of electron bunches. To address this challenge, we use a Radio Frequency Compression system, which is detailed in the next section.

1.2.1.3 Radio frequency Compression

Ultrashort electron pulses ($<$1ps duration) are essential for ultrafast electron scattering experiments but are more challenging to obtain. Electrons within the pulse exhibit electrostatic repulsion, where those at the leading edge experience acceleration due to the lagging net charge, while those at the trailing edge undergo deceleration [16]. The extent of pulse broadening is contingent upon various parameters, encompassing the electron count within the pulse, the transverse spatial width of the pulse, and the initial temporal duration of the pulse. The solution implemented by Morrison and

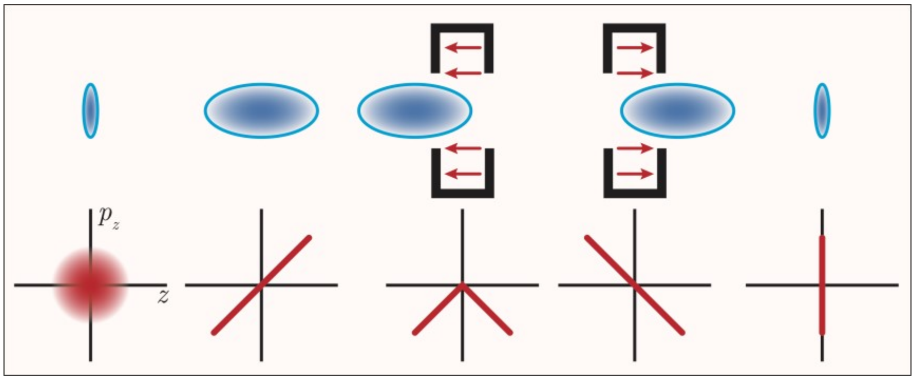

Figure 1.3: Schematic of phase space distribution using RF compression cavity. The propagation of the initially uncorrelated electron pulse leads to the development of a linear longitudinal phase-space relationship. As the pulse moves through the RF cavity, the distribution is turned around. Then, as it moves towards the sample, it compresses ballistically.

Chatelain [17], which was later redesigned and improved by Martin Otto [18], is provided here. As a pulse propagates and extends, it undergoes the development of a linear position-momentum correlation, commonly referred to as a chirp.

A radio frequency cavity operating in a TM010 mode can be employed to mitigate the expansion of the electron pulse. By application of time dependent longitudinal electric field with the propagation of the electron pulse, one may invert its linear chirp. By doing so, the electron pulse collapses to its initial configuration a fixed time later, affecting the desired short pulse duration. As shown in the Schematic 1.3 of the approximate electric fields required to invert the phase space character of the pulse to induce compression during propagation, rather than stretching. The electric field strengths in the cavity used can reach up to 10 MV/m at the center, Similarly, the cavity's resonant frequency varies linearly with temperature, approximately 50 kHz/^{o}C, and so a high-performance recirculating chiller is used.

1.2.1.4 Image Detection System

In order to successfully record and examine ultrafast electron diffraction patterns, an ”ideal” detector camera for UES should have a number of essential features. Originally, the camera should hold the ability to capture images with exceptionally brief exposure durations, preferably within the sub-picosecond realm, to precisely depict the dynamic actions of the materials. Secondly, the camera should maintain a high spatial resolution which can resolve fine details in the diffraction patterns. Thirdly, a wide dynamic range is essential for the detector camera, which should be able to resolve fine details obtained in the range of electron scattering cross-section. Moreover, to enable accurate analysis and interpretation of the diffraction patterns, low noise levels, such as readout noise and dark current, are crucial to ensure that the recorded data is clean and reliable. More importantly, when recording time-resolved sequences, UED experiments generate a large amount of data; therefore detector for UED should have fast readout capabilities. A fast readout makes data acquisition efficient, shortening the interval between measurements and enabling real-time analysis.

Our UED system is equipped with the latest cutting-edge 16-megapixel device that covers a generous image area of 63.5 x 63.5 mm^2. Its remarkable acquisition speed reaches up to 48 frames per second (4k x 4k resolution) or up to 384 frames per second for smaller subareas. These impressive capabilities make this camera the optimal choice for various applications. The incorporation of Dual Readout Technology in the Tem Cam-XF416(ES) further enhances its performance, achieving an exceptional Ultra High Dynamic Range of 20000:1.

1.2.2 Observable in UES experiments

The recorded diffraction images with real-time dynamical changes occurring in atomic lattice precisely at a single vibrational period (10^{-13}s) provide valuable information about the fundamental properties of materials. Following these dynamical changes in time-dependent electron scattered intensities, $I(\vec{q})$, if expanded using a Taylor series, $I(\vec{q}) \approx I_0(\vec{q}) + I_1(\vec{q}) + \ldots$ in the small atomic displacements can be associated with phonons.

$$I(\vec{q}) = I_0(\vec{q}) + I_1(\vec{q}) + I_2(\vec{q}) + \ldots \tag{1.1}$$

$$I_0(\mathbf{q}) \propto \delta(\mathbf{q} - \mathbf{G}) \left| \sum_a f_a(\mathbf{q}) \exp\left[-M_\alpha(\mathbf{q})\right] \exp\left(-i\mathbf{q} \cdot \mathbf{r}_\alpha\right) \right|^2 \tag{1.2}$$

The above equation(1.1) consists of the scattering contributions into Bragg and diffused scattering components, representing the intensity of the scattered electron beam at a wavevector $\vec{q}$ as a sum of multiple terms. Each term, $I_n(\vec{q})$ (as n= 0,1,2,...), corresponds to the contribution of different scattering processes. Equation (1.2) $I_0(\vec{q})$ represents the Zeroth-order elastic Bragg scattering contribution. The delta function $\delta(\mathbf{q}-\mathbf{G})$ enforces the Laue condition in single-crystal diffraction. The Laue conditions relate to the geometry of the crystal lattice and the wavelength of the incident radiation. They can be formulated in terms of the lattice vectors of the crystal and the change in the wave vector of the incident radiation. Specifically, they state that for constructive interference (which leads to diffraction) to occur, the difference in path length between radiation scattered from different lattice planes must be an integer multiple of the incident radiation wavelength. Mathematically, the Laue conditions can be expressed as:

$$\vec{a}_i \cdot (\vec{k}_f - \vec{k}_i) = h_i \lambda \tag{1.3}$$

where $\vec{a}_i$ are the lattice vectors of the crystal, $\vec{k}_i$ and $\vec{k}_f$ are the wave vectors of the incident and diffracted radiation, h_i are integers (miller indices), and λ is the wavelength of the radiation. Therefore, function $I_0(\vec{q})$ and the delta function $\delta(\mathbf{q}-\mathbf{G})$ are used to describe the intensity of the diffracted radiations and to ensure that the scattering is only significant when the Laue conditions are satisfied. At any temperature above absolute zero, atoms in a solid vibrate around their equilibrium positions. These vibrations become more pronounced at higher temperatures. The physics of these vibrations can be described by the Debye-Waller factor in a crystal lattice. The term Debye-Waller $\exp\left[-M_\alpha(\mathbf{q})\right]$ observed to be dependent on $M_\alpha(\mathbf{q})$ that is give as

$$M_a(\mathbf{q}) = \frac{1}{4m_a} \int \frac{d\mathbf{k}}{(2\pi)^3} \sum_j \left|a_{j,\mathbf{k}}\right|^2 \left|\mathbf{q} \cdot \hat{\mathbf{e}}_{j,a,\mathbf{k}}\right|^2 \tag{1.4}$$

Here the direction of polarization is defined by phonon eigenvector $\mathbf{e}_{j,a,\mathbf{k}}$ associated with phonon frequency. The modulus amplitude $a_{j.\mathbf{k}}$ is associated with the quantum number $n_{j,\mathbf{k}}$, the number of phonons associated with that specific index within field: $\left|a_{j,\mathbf{k}}\right|^2 = \left(h/m_{\mathrm{q}}\omega_{j,\mathbf{k}}\right)\left(n_{j,\mathbf{k}} + 1/2\right)$. The Debye-Waller factors suppress the structure factor and is dependent on the magnitude of atomic displacement linked to all phonon modes. The equation (1.4) can be reduce to first order $M_a(\mathbf{q}) = 2\pi^2 \left\langle u_a^2 \right\rangle q^2$ in the range of atomic displacements. Within this range, the amplitude of the squared scattering vector and the mean-square atomic displacements are also important factors in the attenuation of Bragg-peak intensities.

$$I_1(\mathbf{q}) \propto \sum_j \frac{n_{j,q-\mathrm{G}} + 1/2}{\omega_{j,\mathbf{G}-\mathrm{G}}} \left|F_{1j}(\mathbf{q})\right|^2 \tag{1.5}$$

Again, referring from equation(1.1), the first order term $I_1(\mathbf{q})$ can be written as equation(1.5) which is known as phonon diffuse scattering intensity [1]. Where, $F_{1j}(\mathbf{s})$ is named as single-phonon structure factor, which is written as

$$F_{1j}(\mathbf{q}) = \sum_a \frac{f_\alpha(\mathbf{q})}{\sqrt{m_a}} \exp\left[-M_a(\mathbf{q})\right] \left(\mathbf{q} \cdot \hat{\mathbf{e}}_{j,q,s-G}\right) \exp\left(-i\mathbf{q} \cdot \mathbf{r}_a\right). \tag{1.6}$$

The scattering I_1 at $\mathbf{q}$ results solely from phonon excitations with a wave vector $\mathbf{k} = \mathbf{s} - \mathbf{G}$, where $\mathbf{G}$ represents the reciprocal lattice vector linked to the nearest Bragg peak to the scattering vector $\mathbf{q}$. Consequently, I_{I} provides momentum-resolved insights into the crystal's phonon excitations. The zeroth and first-order scattering contributions are the most dominant in our diffraction pattern, representing the coherent scattering from the periodic lattice of the materials (zeroth-order) and the diffused scattering arising from atomic displacements (first-order), respectively.

Higher-order terms in the scattering series, while less intense, contain information about more complex processes such as multi-phonon excitations and higher-order electron correlations. However, these terms are often neglected due to their significantly lower intensity compared to the zeroth and first-order terms. Quantitatively, the intensity of higher-order terms falls off rapidly due to factors such as the decrease in cross-section for higher-order processes and increased susceptibility to incoherent effects and noise. In most ultrafast electron scattering (UES) applications, the primary focus is on the structural and dynamical characteristics of materials, which are adequately described by the zeroth and first-order intensities. These orders provide fundamental knowledge regarding the lattice structure, atomic displacements, and phonon dynamics. Thus, while higher-order terms can offer deeper insights into complex physical phenomena, their practical significance is often limited in the context of UES studies due to their reduced intensity and greater vulnerability to experimental uncertainties.

1.2.3 Sample Requirement for UES Experiments

The scattering patterns and diffraction from UES experiments results are greatly influenced by the sample's geometric properties. To ensure accurate and meaningful results, the samples employed must possess ultra-thin characteristics, ideally on the order of tens of nanometers for single crystal specimens. This thinness is pivotal to mitigating the impact of multiple scattering events, allowing the acquired ultrafast electron diffraction (UED) data to be interpreted within the kinematic scattering approximation. Secondly, the samples must exhibit well-defined lateral dimensions, typically exceeding 250 microns. Ideally, it is preferable for the specimens to match the electron beam's size at the sample in the sample chamber, which (beam) is roughly 500 microns. For more precise observations, the electron beam can be apertured down to produce a smaller spot size, but at the cost of a reduced signal.

Thirdly, when the specimen is continuously exposed to intense laser shots during the experiment, heat can accumulate in the pumped region of the specimen. This heat buildup can affect the specimen's properties, especially if temperature is a key consideration, such as studying phase transitions that occur at a specific critical temperature (T_c). To mitigate the specimen's integrity, the management of thermal dissipation is important and may require totally customized solutions for specimen preparation and mounting.

Fourthly, sample's homogeneity is essential for obtaining consistent and reproducible UES results. Homogeneous samples provide an accurate characterization of the material's structural dynamics by minimizing variances in diffraction patterns. Chapter 2 will further discuss the significant details regarding tools and techniques to acquire ideal samples for UED/UES experiments.

Last but not least challenge is associated with standard substrates that have been manufactured and used to support specimens that are transparent to transmission electron microscopes. Once the desired samples are obtained, the subsequent step of transferring these samples onto the appropriate substrate becomes a critical undertaking. Examples of metallic grids to support films and ultrathin flakes, silicon nitride membrane windows, and amorphous carbon apertures are shown in Figure. 1.4. Additionally, choosing a substrate is a strategic option in itself because each substrate

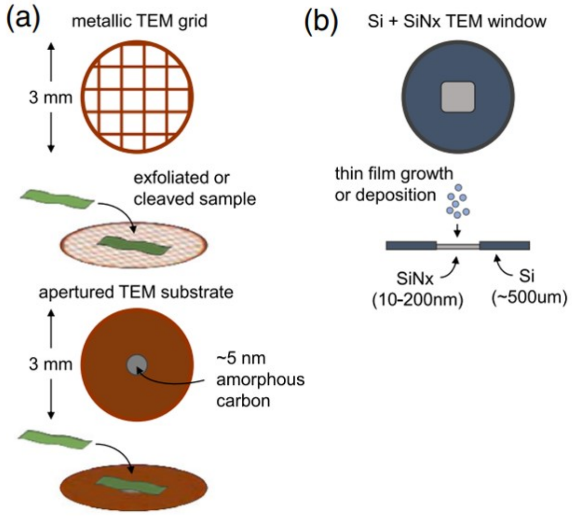

Figure 1.4: Types of sample substrate (a) TEM metallic grid with 3mm diameter of mesh, bottom shows metallic single hole carbon supported TEM substrate, (b) shows single hole (Silicon: Nitride) Si:N layered TEM window/substrate [1].

has its own advantages and considerations. Copper mesh grids are appropriate for quick screening because they allow for imaging up to high-order scattering at once, can resist greater beam currents, and provide better thermal conduction. Contrarily, single-hole Silicon Nitride (Si:N) assembled grids offer superior imaging conditions for distinct, well-isolated samples and permit high-resolution imaging without substrate interference. Getting desired samples on such substrates is an issue that needs to be addressed [19].

Achieving such extremely specified samples is a core challenge, often requiring meticulous preparation techniques and cutting-edge fabrication methods. We provide a novel approach in Chapter 2 to address the abovementioned challenges.

1.3 Sample Characterization for UES experiments

Prior to doing ultrafast electron scattering investigations, sample characterization is crucial because it offers important details about the sample's structure and properties. This compulsory step ensures to produce correct and significant results, preventing erroneous conclusions and improving the trustworthiness of the data obtained. To better understand this significance, let's delve into the example of a single crystal sample. Take, for instance, a two-dimensional (2D) material – confirming whether it consists of mono- or few-layers, or whether the sample is homogeneous or not is of paramount importance. Considering another example of samples prepared via Pulsed Laser Deposition (PLD), The precise identification of crystalline phases and crystallographic orientations becomes essential to ensure that the intended material properties are preserved throughout the PLD process. Such meticulous verifications are conducted by Raman spectroscopy and Transmission Electron Microscopic (TEM) technique in this thesis. This not only bolsters confidence in the subsequent UES experiments but also underpins the credibility of the obtained results.

1.3.1 Introduction to Raman Spectroscopy

This approach is commonly used to identify molecular vibrational modes in materials, although rotational and other low-frequency modes of systems can also be determined with the help of this technique [20]. This technique is extremely sensitive to bonding and geometric structure of materials. Therefore, a slight difference in the geometric structure leads to significant differences in the observed Raman spectrum. Considering the ability to detect subtle variations in geometric structures proves advantageous for examining the thickness of several 2D material thin films. The practical implementation of this technique will be discussed in chapter 2; here we will address the instrument's fundamentals and technical aspects. A monochromatic light source interacts with a material's lattice vibrations in the system, resulting in inelastic scattering and deformation of its electronic cloud. The simplest understanding of this interaction can be given as following equation(1.7)

$$\hbar\omega_s = \hbar\omega_i \mp \hbar\omega_p \tag{1.7}$$

where $\hbar$ denotes the reduced Planck constant, while ω_i, ω_s, and ω_p correspond to the frequencies of the incident photon, the scattered photon, and the light's phonon, respectively [20]. The deformation in electronic potential leads to a change in the polarizability of molecular bonds (details in section 1.3.5). Incident photon excitation puts molecules or atoms into a new virtual energy states for a short interval of time. If the energy of the emitted photons is not equal to the incident photons it is called inelastic scattering. which gives rise to active Raman modes. Although Raman spectroscopy possesses the capability to detect polar bonds, such as Carbon-Oxygen, its sensitivity is predominantly oriented towards homonuclear molecular bonds like Carbon-Carbon, Oxygen-Oxygen, and Nitrogen-Nitrogen, due to the intricate nature of its detection mechanism.

The standard Raman instrument is composed of three major components. First, the instrument must have a monochromatic light source in the range of 400nm to 800nm. This is usually composed of one or more lasers. The important restriction for the illumination system is that the material or solvent should not absorb the incident frequency of light. The second major part is the sample illumination system. The degree of variation in these parameters depends significantly on the instrument's configuration, encompassing distinctions between standard macro-Raman and micro-Raman systems. The phase of the investigated material is typically determined by the sample illumination. The final integral component of a Raman system is the spectrometer, typically situated at a 90° angle relative to the incident illumination. It might incorporate a set of filters or a monochromator to refine spectral characteristics. Modern Raman uses array detectors such as CCDs, which are significantly useful for weak signal detection. To separate the Raman scattered light from the Rayleigh signal, the instrument must have a long pass filter or notch filter as shown in schematic 1.5. These filters have spectral resolution upto 5 cm^{-1} [21].

1.3.2 Rayleigh Scattering

During the elastic scattering, The incident photon ($\hbar\omega_i$) is momentarily absorbed by an atom, exciting it into a new virtual state. A virtual state is a transient, higher-energy state that is not directly observable in the material's ground state. After a small interval of time when de-excitation takes place from the virtual to state back to its original state, where the emitted photon's energy remains unchanged, is called Rayleigh scattering as shown in Figure 1.6. Its also called the two-photon process involving the scattering of incident light from a virtual state.

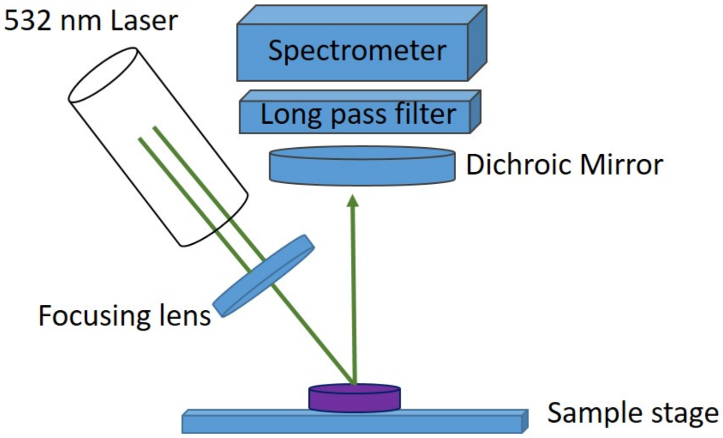

Figure 1.5: Instrumental schematic of Raman spectrometer, The laser (532 nm) is focused onto a sample using a focusing lens, and the Raman scattering signals are collected through a dichroic mirror which passes through a long pass filter and read by the spectrometer.

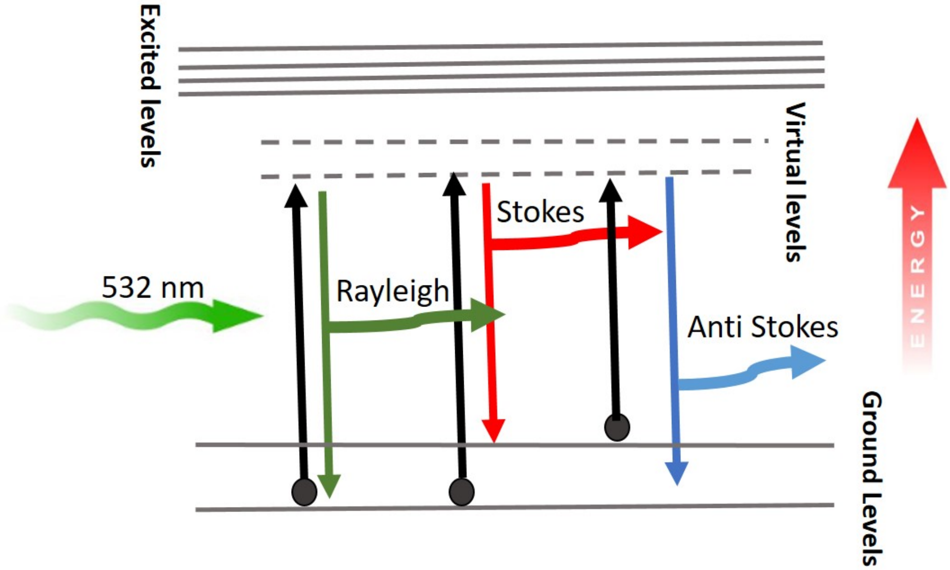

Figure 1.6: Energy diagram of Rayleigh, Stokes, and anti-Stokes Raman scattering. Photons from laser (532 nm) interact with lattice promoting the atoms to short-lived virtual energy levels. De-excitation to different ground levels is responsible for Rayleigh, Stokes, and anti-Stokes scatterings.

1.3.3 Stokes Scattering

The phenomenon involves the interaction of incident light with the vibrational modes of the lattice. When a photon interacts with the solid material, it imparts energy to the lattice, promoting it to a virtual state. Subsequently, the solid material relaxes, and the lattice vibrations return to a higher vibrational state compared to their initial equilibrium positions. The solid releases a scattered photon with energy h-E during this relaxing process, where h is Planck's constant and E is the energy of the vibrations of the lattice in the higher vibrational state. The energy exchange that took place between the lattice vibrations and the incident photon is indicated by the energy difference (h-E) between the incident photon and the scattered photon. This energy exchange causes the photon to scatter inelastically, and the Raman Stokes lines that are visible in the scattered light provide important details on the lattice vibrations and their corresponding vibrational energies.

1.3.4 Anti-Stokes Scattering

The anti-Stokes process is exactly the opposite of the Stokes process; as we know that the Stokes process involves the emission of a photon with lower energy (lower frequency) due to the relaxation of a lattice from an excited virtual state to an upper vibrational state, the anti-Stokes process involves the emission of a photon with higher energy (or frequency).

In the case of anti-Stokes Raman scattering, the molecule or lattice is initially in its excited state, and it absorbs a photon with energy hν . This absorption of energy excites the molecule or lattice to virtual states as shown in Figure 1.6. The molecule or lattice then relaxes back to the lowest vibrational state from its initial state and emits a scattered photon with energy h(ν+$\Delta\nu$), where $\Delta\nu$ is the frequency shift associated with the vibrational transition. The anti-stokes lines are observed to be less intense because they involve the higher vibrational states, however it can still provide valuable information about certain high-frequency vibration modes and higher states of energy.

1.3.5 Observable in Raman measurement

In order to understand the complete picture, one may need to understand both classical and quantum models of Raman spectroscopy. Classically, the Raman scattering is known as Rayleigh effect, which is strictly associated with lattice or molecular vibrations polarizability factor. if E is traveling light wave at frequency ω_p

$$E_i = E_0 \cos(\omega_p t) \tag{1.8}$$

Microscopic polarisation of the lattice can be given as, $p = \varepsilon_0 \alpha E_i$ where α is microscopic susceptibility, which can be written as

$$\alpha = \alpha_0 + \left.\frac{d\alpha}{dQ}\right|_0 Q + \cdots \tag{1.9}$$

considering the generalised coordinate, $Q = Q_0 \cos(\Omega t)$ and substituting for α, Q and E_i,

$$p = \varepsilon_0 \left[\alpha_0 + \left.\frac{d\alpha}{dQ}\right|_0 Q\right] E_0 \cos(\omega_p t) \tag{1.10}$$

and separating the components we get our final equation of polarizability,

$$p = \varepsilon_0 \alpha_0 E_0 \cos(\omega_p t) + \frac{\varepsilon_0 Q_0}{2} \left.\frac{d\alpha}{dQ}\right|_0 \left[\cos(\omega_p + \Omega) t + \cos(\omega_p - \Omega) t\right] \tag{1.11}$$

From the above equation, Ω is known as the Raman shift or Rayleigh scattering of the incident light. The Rayleigh-Raman (elastic) scattering equation for the intensity of the scattered light, is given as:

$$I_s \propto |\alpha \cdot \mathbf{E}_i|^2 \tag{1.12}$$

The quantum mechanical description of Raman scattering is derived from the quantum mechanical perturbation theory and is known as the Raman scattering cross-section equation. which is given as

$$\sigma_{\text{Raman}} \propto \left| \sum_i \frac{\mathbf{d}_{i0} \cdot \mathbf{E}_0}{E_0 - E_i} \right|^2 \tag{1.13}$$

Where σ_{Raman} is the probability of Raman scattering crosssection, $\mathbf{d}_{i0}$ is the transition dipole moment between initial and intermediate states, in the above equation $\mathbf{E}_0$ and $\mathbf{E}_i$ are represented as the energy of these states. The equation involves a sum over all possible intermediate states, and the cross-section depends on the transition dipole moments between the initial and intermediate states. So far, the recorded spectral range for vibrations is approximately 5 to 3500 cm^{-1}.

Chapter Summary

Ultrafast Electron Scattering (UES) stands out as an unparalleled tool that offers real-time direct visualization of materials dynamics. This dynamic examination of materials sheds light on their response to external stimuli, transient phase switch, and transient electronic states. Such an advantage outperforms the capability of any current analytical method. However, it is critical to emphasise the requirement that the samples used in UES research must adhere to strict guidelines. The performance of UES depends on the sample's suitability, which includes elements like its size, shape, thickness, and structural quality. Ideally, the samples should possess well-defined lateral dimensions, ensuring that the scattering patterns obtained are interpretable and yield meaningful insights. To prevent unwanted multiple scattering issues, samples must be thin enough to enable accurate data interpretation. We also underscore the critical significance of post-sample preparation characterization in pursuing accurate and meaningful experimental outcomes.

Chapter 2

Disassembling of 2D Van dar waals Crystals for UES experiments

The investigation of lattice dynamics following photoexcitation by a femtosecond laser pulse is crucial to the research of nonequilibrium phenomena in solid-state systems. Despite remarkable progress in understanding such phenomena, the approach can only be applied to materials that can be suitably prepared for interrogation by UES. There has been a recently explosion of interest in layered (or 2D) materials, and this class of materials is particularly well suited to preparing high quality, nm thick crystal flakes. The following chapter provides a detailed picture of my experimental approach, conducting an efficient, versatile method that yields high-quality, laterally extended ($\geq 200\mu m$)*, and ultra-thin* (≤ 5 *nm) single crystals layers on metallic Transmission Electron Microscopic (TEM) mesh grides and on Silicon Nitride (Si:N) TEM single windows substrates.*

2.1 Conventional Approach and Contemporary Challenges in Sample Preparation

In the context of UES experiments, Importance of ideal samples, as addressed in the previous Section 1.2.3, becomes more pronounced. It is imperative to have well-prepared samples that meet the stringent requirements for UES experiments. The demand for sample preparation techniques out-

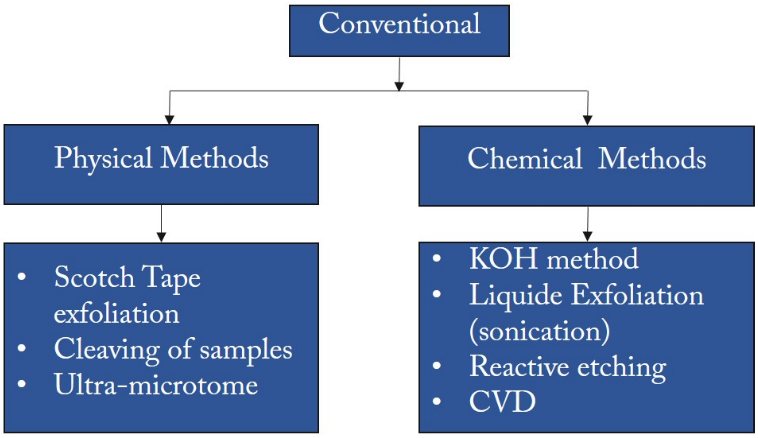

Figure 2.1: Flow chart of conventional sample preparation techniques for application in TEM.

bursted with the initial discovery of monolayer graphene in 2004 [22]. Single-layer or multi-layer atomically stacked structures compose 2D layered materials. Van der Waals (vdW) forces impact each layer, and strong covalent bonding controls atomic interactions within a layer. Due to such weak interactions between the layers, It has been possible to peel off each layer from the bulk crystals by using a plane scotch tape. The knowledge regarding the fundamental structure is encrypted in those thin exfoliated layers, which can unlock the material's full potential for several commercial applications. A flowchart Figure 2.1, represents some conventional approaches to obtaining thin layers from bulk crystals. Scotch tape exfoliation, sample cleaving, and ultramicrotome are examples of physical procedures; similarly, chemical methods include the KOH (Potassium Hydroxide) process, ultrasonication, and CVD (Chemical Vapor Deposition). It's crucial to go through some of the specifics of chemical and physical processes because doing so opens up the possibility of addressing contemporary challenges and creating new, effective methods for high-quality samples for UES experiments.

2.1.1 Chemical Methods

In the past, various research using a chemical method has been carried out to produce layers of 2D materials [23, 24, 25]. Some of the most practiced techniques are liquid exfoliation [2], and method with potassium hydroxide (KOH) [26], although demonstrated great outcomes, but found quite difficult upon layers transferring to substrate out of solutions. Similarly, continuous monolayers may be grown by CVD on wafer scales; their performance in electronic devices is limited due to the polycrystalline forms with high defect density in layers. Let's take an example to understand how chemical exfoliation works. In the process of intercalation, chemical ionic species, extands the interlayer separation by diminishing interlayer cohesion and lowering the energy hurdle for exfoliation in material. As demonstrated in Figure 2.2 consider yellow balls are ions. Ions are intercalated between layers of materials in a liquid environment, the materials start swelling, and the weakening of interlayer separation takes place. The primary driving force for ion intercalation is the electrostatic attraction between the ions in the solution (such as KOH) and the layers of the material. For instance, if the layers are negatively charged, they will attract and accommodate positively charged ions (cations) from the solution. Diffusion also plays a role, as ions move from an area of higher concentration (in the solution) to an area of lower concentration (between the layers), seeking to achieve equilibrium. The role of the solvent (in this case, water in the KOH solution) can also be significant. Solvent molecules can assist in the intercalation process by solvating the ions and helping to transport them into the interlayer spaces. In some cases, osmotic pressure can also contribute, especially if there is a significant concentration of ions. This pressure can help in pushing the ions into the interlayer spaces. Another technique of using sonication in solvents for the exfoliation of layered materials, though involving a physical process (sonication), is often classified as a part of chemical exfoliation methods. This categorization is due to the overall process incorporating both physical and chemical aspects to achieve exfoliation. The layered materials are sonicated in solvents. Sonic waves generate cavitation bubbles; when that bubble collapses, it bursts out high energy compared to the thrust of a jet engine, which causes the breaking of layered materials. UES imaging of the atomic structure of oxidation-sensitive transition metal dichalcogenides (TMDs), when prepared with the KOH method, is very difficult. The challenge here is such a chemical approach can introduce impurities/defects and contaminants from the chemicals used in the exfoliation process, which can negatively alternate layers properties that are not acceptable for expected UES experiments.

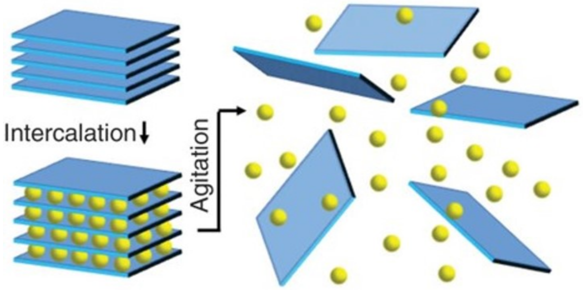

Figure 2.2: One example schematic of chemical (KOH) exfoliation, where Ions intercalate within material's layers swelling takes place that cause separation of layers [2].

2.1.2 Physical Methods

Physical methods to obtain exfoliated layers from high-quality bulk crystals can currently produce top-quality monolayers; however, the typical lateral dimensions are (<100 μm), with very low yield. For example, exfoliating graphite with scotch tape many times will split the flakes into small pieces, which makes it hard to produce ~ 500 micron monolayer graphene.

Ultramicrotome is another valuable physical method to produce layers with submicron precision. The first step involves preparing the sample to be sectioned. This often includes embedding the sample in a resin to stabilize it and make it easier to cut. The resin is hardened, encasing the sample in a block. The sample block is then mounted in the ultramicrotome. A very sharp blade, typically made of diamond, is used to slice the sample. The ultramicrotome can be adjusted to slice at varying thicknesses, often as thin as a few nanometers. This precision is crucial for obtaining high-resolution images, especially in electron microscopy. The delicate nature of the technique demands careful and meticulous handling, which can extend the sample preparation time. My several attempts during the ultramicrotoming and scotch tape exfoliation process with slightly strong vdW force materials, such as $TiSe_2$ or $SnSe_2$, are found to be susceptible to cracking or fracturing.

In past within the Siwick group a Crystalbond sample exfoliation technique was employed to achieve the desired layers. In this technique, bulk crystal is glued to a 3mm copper mesh TEM grid, The grid itself is attached to a glass slide with the same transparent glue. This transparent Crystalbond-509 glue (SPI supplies) is dissolvable in Aceton/Isopropanol. The glued bulk crystal is exfoliated repeatedly with simple scotch tape until it becomes translucent to the naked eye. The Crystalbond is then carefully removed with acetone, applying one drop at a time via a glass pipette until the TEM grid/substrate is freed from the glass slide. The biggest drawback of this technique was once you obtain the thin layer, the probability of breaking it becomes high while removing unwanted glue from the TEM grid/substrate. Moreover, high surface tension of aceton was another factor that makes this process intolerable to achieve a few nanometer thin layers with large laterals.

2.2 Advancements in Sample Preparation Techniques at Siwick Lab

Recently, an innovative approach to obtain a few layers of single crystals with sufficient size and lateral dimensions have been shown by one of our collaborators [27] at Columbia University, USA. They reported that some metals (e.g. gold) had a strong adhesion with TMDCs. Upon exfoliation, it can repeatedly produce complete single-crystal layers, each acquiring huge lateral dimensions nearly the size of the bulk mother crystals.

Inspired by their approach, at Centre for the Physics of Materials (CPM) McGill University, I was successfully able to setup a similar technique but with major modifications. In our technique, with the help of e-beam evaporation (0.05 nm/s), a 150 nm-thick Au (gold) film was deposited onto an ultrasonicated and clean Si wafer as shown in schematic 2.3 Step 1. PVP (Polyvinylpyrrolidone) solution (from Sigma Aldrich, mw 40000, 10% wt in ethanol/acetone wt% 1/1) was spin-coated on the top of the Au film (1200 rpm, acceleration 500 rpm/s, 3 min) in Step 2. The role of PVP here is to act as an adhesive layer that facilitates the transfer of thin films. PVP provides a uniform and stable surface for subsequent steps and ensures the integrity of the thin layers during the transfer process.

A piece of TRT (Thermal Release Tape) was used in Step 3 to pick up the PVP+Au coated film from the Si substrate, as shown in Fig. 2.3. The TRT is essential for this technique as it enables the easy and damage-free transfer of thin films. Its thermal release properties allow for the gentle removal of the film without causing any mechanical stress or damage to the delicate layers.

Roughly a ∼300-400 nm thick mother crystal was used in Step 4 to gently peel off the desired thin layers. The TRT is gently lifted up in Step 5, with mono/bi/tri-layers expected to be attached on top of the Au-assisted tape. In Step 6, a substrate (Cu) mesh grid is introduced in a petri dish slightly filled with diluted isopropanol. As shown in step 7 (Fig. 2.3), the ultrathin layer was then transferred by dipping the PVP/Au film with monolayer in diluted isopropanol solution, onto a Cu (copper) mesh grid TEM substrate.

In the schematic 2.3, we only show the Cu mesh grid for visual understanding; depending on the need, one can also use silicon nitride (Si:N) (Norcada) TEM single window substrates. It's important to note the major difference between our method and the previously reported case where the TRT was removed by heating at 120°C, and the PVP layer was removed by dissolving in deionized (DI) water. Here instead, we used a diluted isopropyl solution to remove all Au-assisted TRT with the PVP layer at the same time. The evaporation and adhesion force of the liquid bring the Cu grid of the TEM in contact with the desired layer. We used an eyelashes pen to gently split the desired layer from Au-assisted tape, the petri dish was then dried off under N_2 flow and kimwipes, which makes the desired layered sample available for use in UES experiments. The layer of gold (Au) occasionally undergoes complete disintegration, while in certain instances, it remains adhered to the tape, and only the desired layer gets separated. Depending on the material's nature, another observation was made that the adhesiveness of the Au with desired layers also weakened down just by coming in contact with the Isopropanol solution. Step 8 is very critical, to transfer the desired layers on top of the substrate, we carefully paddle the solution in the direction of the placed substrate, or sometimes a gentle push around the corner of layers, both worked well to bring the sample in contact with the substrate by help of an eyelash wire holder. It is questionable that while exfoliation from gold tape, Why does one expect mono/bi/tri layers, why not half the crystal? To answer this we consider the following points:

- In 2D layered materials, the layers are held together with der Waals Forces, These forces are relatively weak then covalent or ionic bonds within the layers. Therefore, materials can be easily cleaved along the layers. However, the force required to peel off a few layers is much less than that needed to split the crystal in half.
- The exfoliation process is influenced by the surface energy of the materials involved. The gold-assisted tape likely has a surface energy that interacts favorably with the outermost layers of the crystal, allowing for the adhesion and subsequent peeling off of only a few layers. The energy required to peel off more layers increases, making it less likely.
- The mother crystal's thickness (300-400 nm) suggests it's already quite thin. The forces applied during exfoliation are generally controlled to ensure that only the topmost layers are removed. Too much force would risk damaging the crystal and the thin layers.
- The exfoliation technique, particularly when done manually, relies on the skill and control of the operator. Gentle lifting with controlled force is more likely to yield thinner layers. A more aggressive approach might remove more material, but with less precision and potentially more damage.
- The mechanical strength of the individual layers and their interaction with the tape is a factor. The first few layers might adhere to the tape more readily and can be exfoliated without disturbing the underlying layers. As you go deeper into the crystal, the layers are more tightly bound to each other, requiring greater force for exfoliation.

This method is experimentally demonstrated and systematically explained in the following sections 2.2.1 to 2.2.4 on WS_2 (tungsten disulfide), Graphite, SnS_2 (tin disulfide), and $Bi_2Sr_2CaCu_2O_8$ (BSCCO, or Bi-2212) respectively. Raman characterization, TEM analysis, and UED (ultrafast electron diffraction) measurements were made in order to judge the quality and homogeneity of these thin layers. In addition, this method maintains the possibility of estimating the sample thickness (single-layer or few-layer) before the transfer process onto substrates.

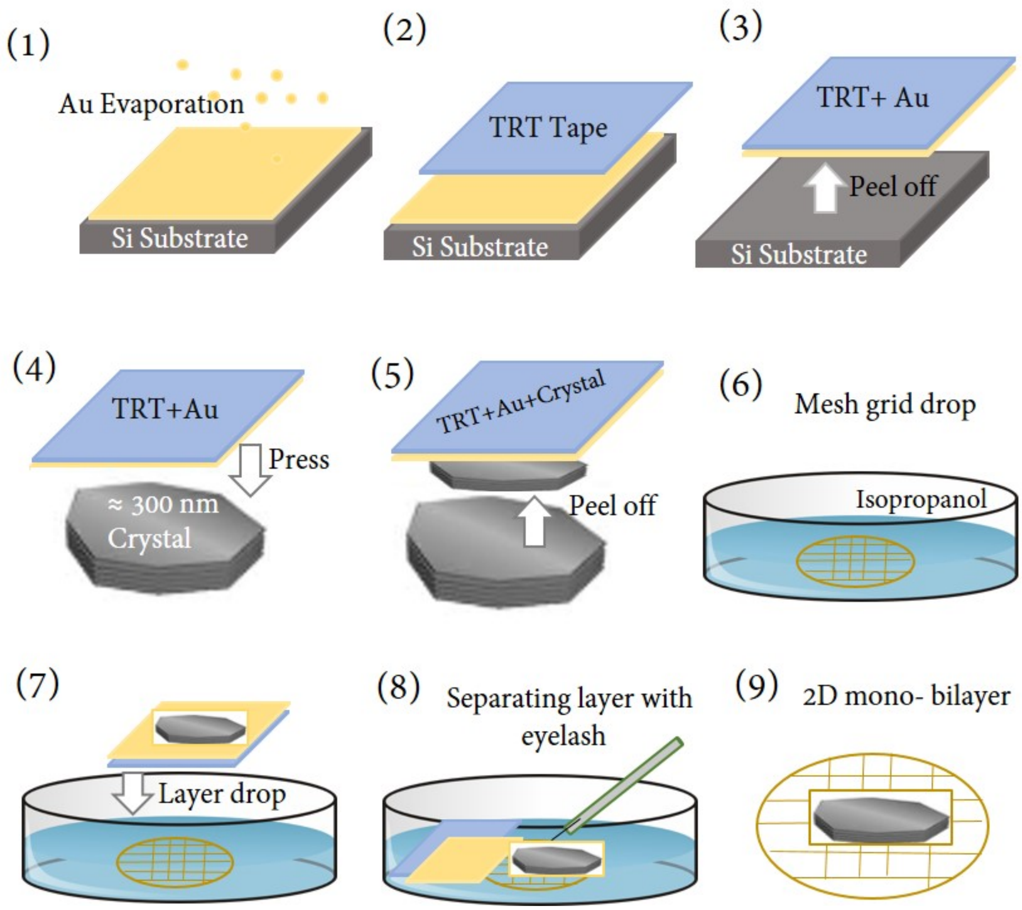

Figure 2.3: Schematic illustration of the layer-by-layer exfoliation procedure of bulk vdW single crystals. (1) Gold evaporation on an ultra-flat silicon wafer (2) using Thermal Release Tape (TRT) to lift the Au+PVP layers (3) peeling off Au-assited TRT tape from silicon substrate (4) Putting the Au tape onto the surface of a $\sim 300nm$ thick mother crystal (5) Peeling off a mono/bilayers with Au tape (6) dropping a Cu mesh grid (TEM) substrate in petri dish filled with diluted Isopropanol (7) Putting the Au tape into a petri dish (8) TRT dissolve glue in 10 minutes and layers get separated by an eyelash pen (9) Petri dish is dried out, and the single-crystal mono/bilayers with macroscopic dimensions are obtained.

For the characterization, a high-resolution TEM (TS Talos F200X) at McGill's Facility for Electron Microscopy Research (FEMR), Ultrafast electron diffraction from Siwick Lab setup (1.2), and Raman spectra were recorded with an alpha 300-R (WITec, Oxford instruments) Raman imaging microscope with a double-frequency Nd:YAG laser (532 nm) as the excitation source.

2.2.1 Implementation on Tungsten Disulfide (WS_2)

Typically, MX2 is used to describe the standard formula of layered TMDs (where **X** = S (sulfur), Se (selenium), Te (Tellurium); and **M** = Mo (Molybdenum), W (Tungsten), Ta (Tantalum), etc.). TMDs are typical layered materials with layers stacked together by weak VanderWaals forces, Just like graphite. WS_2 and MoS_2 are inorganic layered semiconductors with an indirect band gap of ≈ 1.50 eV and ≈ 1.58 eV, respectively [3]. Both WS_2 and MoS_2 exhibit a transition from an indirect gap at multi-layers to a direct-gap at monolayers with an enhancement of quantum efficiency (QE) at a factor greater than 10^3 compared to bulk samples [28]. The figure of Band structure of both materials are shown 2.4, explaining the difference in monolayer and bilayer band's behavior.

WS_2 captures our interest because of its interesting ultrafast time-resolved intervalley dynamics in a monolayer [29], which we can compare to a recent set of experiments performed by our group on monolayer MoS_2 [30]. Hence in this section, we report the optical properties of 2H phase WS_2 (HQ Graphene) mono-, bi-, tri-, quad- and multi-layer of home-prepared (CPM) samples with the help of Raman scattering in the visible range of 532 nm. Although, Raman have been previously employed to study the nature of this material, the Raman scattering of mono- and few-layered WS_2 remains less explored.

Here we recorded a systematical response of single and few-layers WS_2 which defines a general characteristics of those specific phonon modes which are responsible for defining a fingerprint of WS_2 monolayer. For single-layer WS_2, the 532 nm laser excitation (2 mWatt) generates a second-order Raman resonance involving the longitudinal acoustic mode at 174-LA(M), as shown in Figure 2.5. This resonance is the result of the electronic bands and lattice vibrations coupling [31]. The LA(M) mode is similar to sound waves, as their periodic responses are along the direction

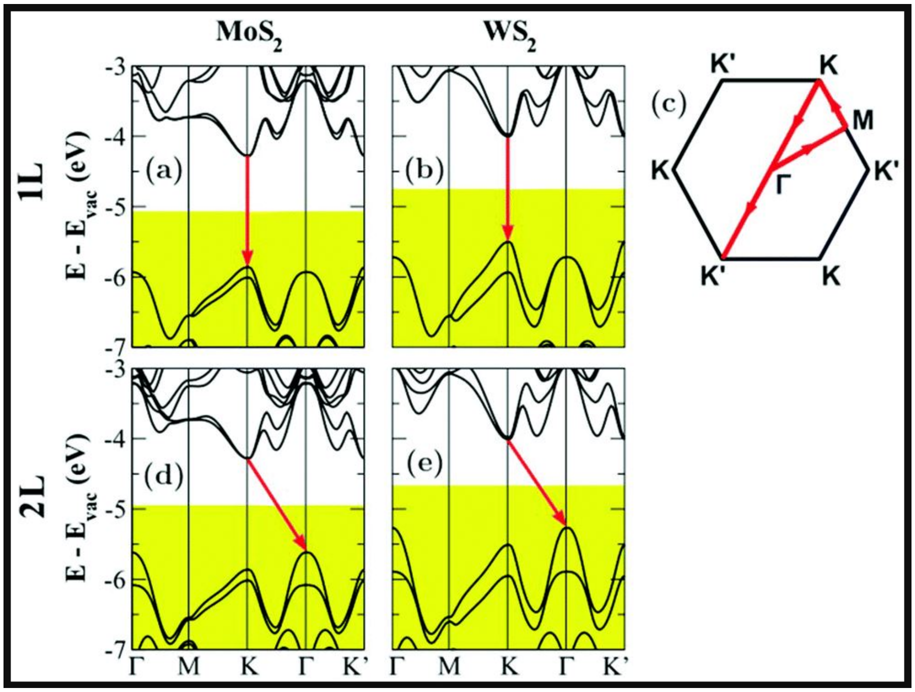

Figure 2.4: Schematic of band structures of (a) MoS_2 monolayer, (b)WS_2 monolayer (d) MoS_2 bilayer, and (e) WS_2 bilayer. (c) A diagram of the Brillouin zone showing the calculation line for band structures, The intersection of the white and yellow sections is where the Fermi energy is located [3].

of propagation. Additional peaks correspond to multi-phonon combinations of these modes [31]. Figure 2.6 presents the Raman spectra range (from 300 to 480cm^{-1}) of WS_2 slabs with layer number N = 1 to 4 and bulk. We can see that E^1_{2g} mode exhibits some reliance on the film thickness, while the A_{1g} mode passes through a blue shift with increasing layer number, indicating a predicted lattice stiffening effect when more layers are added. Looking at the frequency differences ($\Delta\omega$) between the E^1_{2g} mode and A_{1g} mode, the sample thickness could be identified accordingly. These modes have been reported previously in reference literature [31].

Moreover, as shown in Figure 2.7 is the frequency difference as a function of layer number N, I label $\Delta\omega$ = 66.02 cm^{-1}, 66.6 cm^{-1} and 69.5 cm^{-1} to monolayer, bilayer and trilayer respectively. For slabs with four layers or more, $\Delta\omega$ finally arrives at the bulk value around 70.0 cm^{-1}. Distinctly, from monolayer to trilayer the A_{1g} peak is roughly 0.8, 0.70 and 1.0 times the height of the E^1_{2g} peak (Fig. 2.7), proving that the ratio of the intensity of both mode could also provide the

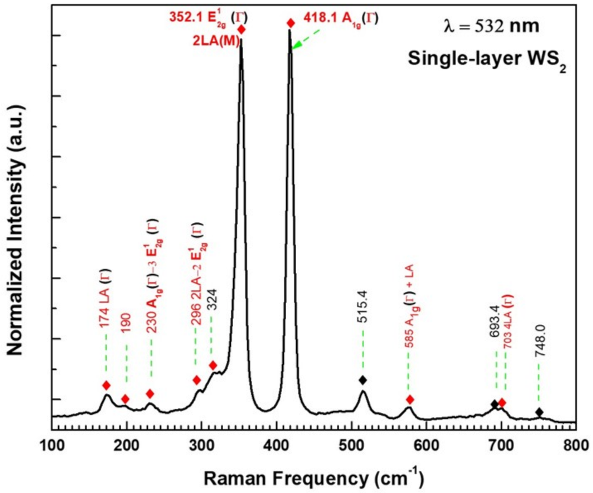

Figure 2.5: Single Raman spectra of Ultrathin WS_2 layer recorded with 532 nm wavelength.

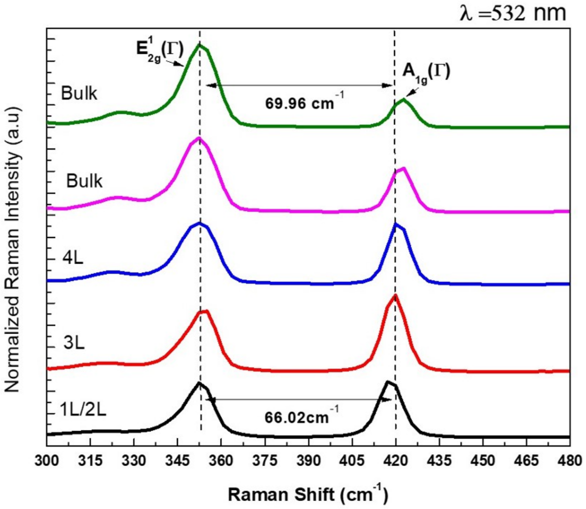

Figure 2.6: Multiple Raman spectras from single layer to bulk WS_2 in the spectrum range of 300 to 480cm^{-1}.

signal for representing sample thickness. The change in the ratio of Raman peak intensities, as well as the frequency shift, can indeed be influenced by the defect density in the material. Defects in the crystal structure can introduce additional vibrational modes or modify existing ones. This can lead to new Raman peaks (defect-induced peaks) or affect the intensities of existing peaks. We did not observe this in our results. However, there is a possibility that some samples may have a high defect density, which could alter the peak intensities and frequency shifts. Thus, these changes might not be solely attributable to variations in layer thickness, but could also be influenced by the presence of defects.

It was found that thin WS_2 single crystals as free-standing mono-layer can't withstand CW laser power in the Raman microscope over 3.5mW, the bulk WS_2 single crystals were less susceptible to laser burn during the measurements as shown in Figure 2.8. The greater susceptibility of the monolayer WS_2 to CW laser damage in Raman spectroscopy is primarily due to factors like reduced heat dissipation, higher optical absorption, mechanical fragility, and possibly the presence of impurities, rather than solely being a matter of sample cleanliness. The manifestation of this damage can be observed both visually and through alterations in the Raman spectral characteristics. The observed wrinkling in the layers during preparation on mesh grid TEM substrates can

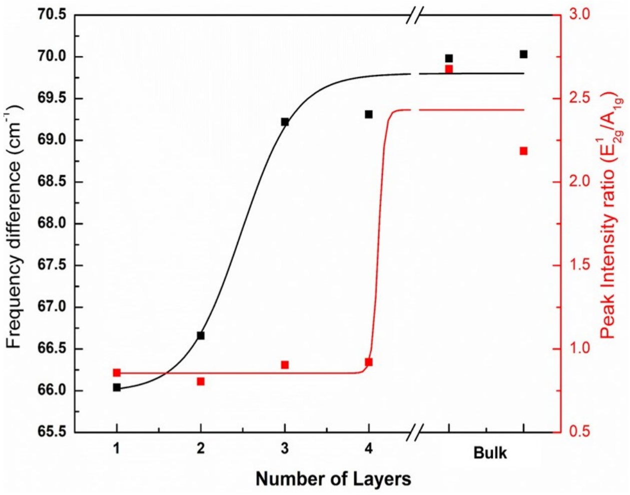

Figure 2.7: The black line represents the variation in frequency, while the red line depicts the change in peak intensity ratio between the E_{2g}^1 and A_{1g} modes with respect to the thickness of the WS_2 film.

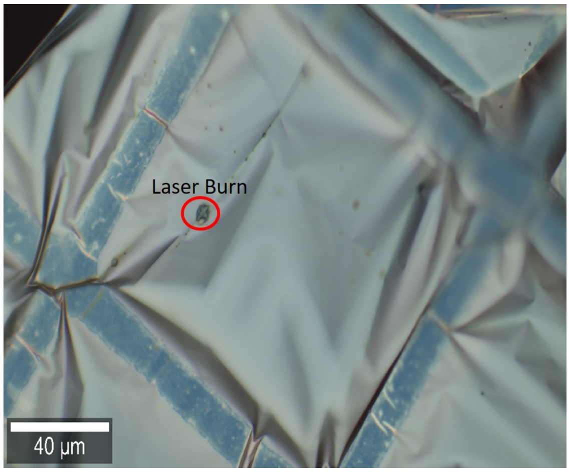

Figure 2.8: Optical microscopic image of a 400-micron flake of monolayer WS_2 on Cu mesh TEM grid, red circle showing laser burn spot.

be attributed to two primary factors. Firstly, these layers are freestanding on the mesh, lacking any supporting structure at the back. This absence of support allows the layers to conform to the underlying mesh topology, leading to the formation of wrinkles. Secondly, the involvement of isopropanol in the process contributes significantly to this phenomenon. As the layers are transferred onto the substrates through an isopropanol medium, the surface tension of the liquid induces wrinkling in the layers. This surface tension effect is particularly pronounced during the drying phase, where differential evaporation rates can lead to uneven stress distribution across the layer, further exacerbating the wrinkling. It is important to note that such physical deformations in the layer structure can have a substantial impact on the material's properties, potentially altering its optical, electrical, and mechanical characteristics. Therefore, understanding and controlling these wrinkling effects are crucial for ensuring the fidelity of the layers for intended applications.

2.2.2 Implementation on Graphite

Graphite consists of AB stacked graphene layers with hexagonal lattice having exotic and unique electronic and structural properties. The layers are held together by a relatively weak Van der Walls interaction produced by a delocalized π-orbital. Previously, one of my seniors, Mark Stern of Siwick group, mapped out the relative EPC (Electon-Phonon Coupling) and PPC (phonon-phonon coupling) strength through their profound sensitivity to photoinduced changes in phonon populations, with Ultrafast diffuse scattering experiments [32]. Currently, to further quench our thirst, with novel UES experiments on Graphite, the Siwick group is preparing the grounds to conduct a second sound experiment in graphite. The second sound is an exotic phenomenon related to heat transport that occurs between ballistic and diffusive transport regimes in layered materials. The researcher Huberman et al. used fast, transient thermal grating measurements to observe the second sound in graphite between 85 and 125 kelvin [33]. The observation of the second sound in graphite is attributed to its layered nature, indicating that this transport mode might be accessible in other 2D materials as well.

Although, Raman spectroscopy has long been used to examine the structural and electrical properties of graphite, revealing important details about defects (D band), in-plane vibration of sp2 carbon atoms (G band), and stacking order (2D band) [34]. In this section, I report the Raman spectrum of mono- and few-layered graphite samples, prepared with gold tape exfoliation technique at CPM. Distinctly, the free-standing samples with lateral dimensions were observed to be $\geq 200\mu$m, comparable with the diameter of an incident electron beam in UES experiments. Figure. 2.9 shows slabs of Raman scattering plot from a mono- (red) and Few- (blue) layered sample analysis. The Raman signal of the monolayer is unexpectedly strong and even comparable to that of bulk graphite. From Fig. 2.9 (blue) we observed that a sharp G peak at $\sim$1590 cm^{-1} and two broad peaks: 2D at $\sim$2790 cm^{-1} and 2D* at $\sim$2724 cm^{-1}, which is typical for high-quality graphite [34, 35]. The G peak represents the high-frequency phonon oscillation of the sp^2 associated with carbon-carbon bonds. The 2D peaks can be considered as the second-order overtones of the 2D* peaks, which are caused by the breathing modes of six-atom rings. Two phonons with

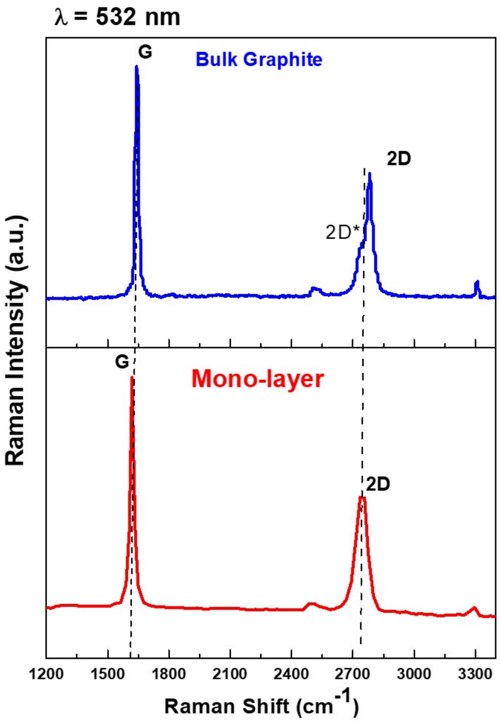

Figure 2.9: Raman spectra of graphene (red) and few layers of graphite (blue) taken with 532 nm laser.

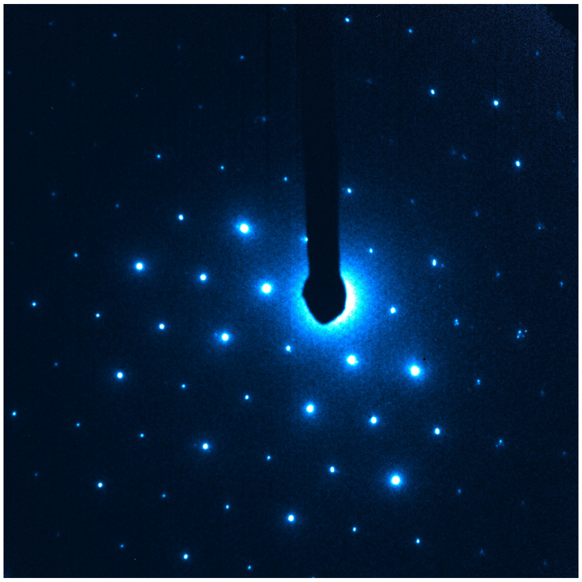

Figure 2.10: Electron diffraction of exfoliated single crystal Graphite Sample prepared at CPM.

opposing wave vectors are involved in the process that gives rise to the 2D peaks. In a perfect sample, momentum conservation would be violated by the double resonance mechanism, and thus the 2D* peak is absent (as observed in Red spectrum) [35]. A static diffraction pattern single crystal Graphite from UES is shown in Figure. 2.10.

2.2.3 Implementation on Tin disulfide (SnS_2)

SnS_2 is trigonal in structure and crystallized in $P6_3mc$ space group with indirect band gap semiconductor, ranging between 2.18 eV (bulk) and 2.41 eV (monolayer) [36]. SnS_2 typically exists in two states, the trigonal (1T) phase being more stable than the hexagonal (2H) phase. While Sn is surrounded octahedrally by six S atoms, two planes of S and Sn atoms positioned between them established a strong covalent bond within the SnS_2 plane. The three atoms per unit cell led

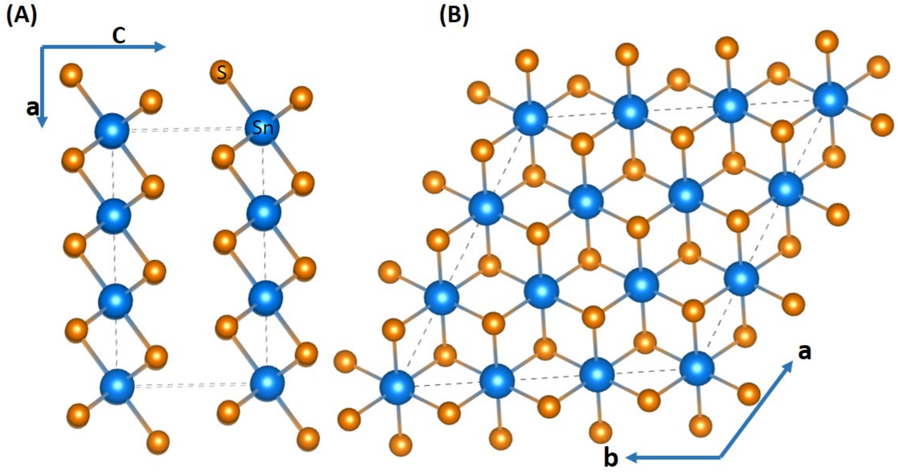

Figure 2.11: Represents (A) side view of SnS_2 where orange ball corresponds to S and blue balls signifies Sn atoms (B) The top view of the optimized 3x3 unit cell SnS_2 structures.

to the creation of the trilayer between the S-Sn-S atoms [36]. Figure 2.11 depicts the structural representation of SnS_2 monolayer in cross-section view along a different crystallographic axis.

Due to lack of appropriate exfoliation techniques, the large scale thin layers of SnS_2 are mostly acquired by CVD technique [37, 38]. In this section, we report the Au-assisted tape exfoliation application on SnS_2 sample prepared at CPM. The Raman spectra of our SnS_2 ranging from 150 cm^{-1} to 400 cm^{-1} under 532 nm excitation, with laser power of 3.5mW are shown in Figure. 2.12. Evidently, A_{1g} phonon mode results from the out-of-plane vibration of the sulfur-tin-sulfur plane of the hexagonal phase SnS_2, which agree with reported positioned on 317 cm^{-1}[39]. E_{1g} phonon mode at 208 cm^{-1} corresponds to thick SnS_2 crystals, As the thickness decreased to couple of nanometer scale, the E_{1g} peak weakened down/disappears, presumably due to the reduction in the scattering centers for in-plane scattering [39, 37]. As thickness decreases from bulk to monolayer, a tiny Red shift in E_1g mode is detected. Consequently, a decrease in vibrational frequency, which can be linked to a decrease in tensile strain provides the proof that the crystal is of good quality. More surprisingly, there was no Raman peak that could be attributed to surface oxidation.

Similar to the case of WS_2, here, Raman shift is slightly sensitive to thickness for 1L-4L, but not for thicker material. Figure 2.13 shows the frequency difference as a function of layer number, intensity label $\Delta\omega$ = 108.5 cm^{-1} and 109.31 cm^{-1} from bulk to monolayer respectively.

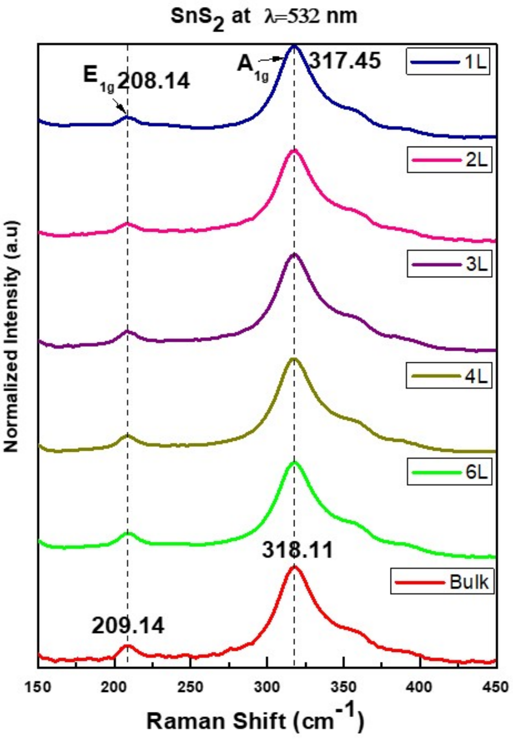

Figure 2.12: Multiple Raman spectras from single layer to bulk SnS_2 in the spectrum range of 150 to 480 cm^{-1}layer

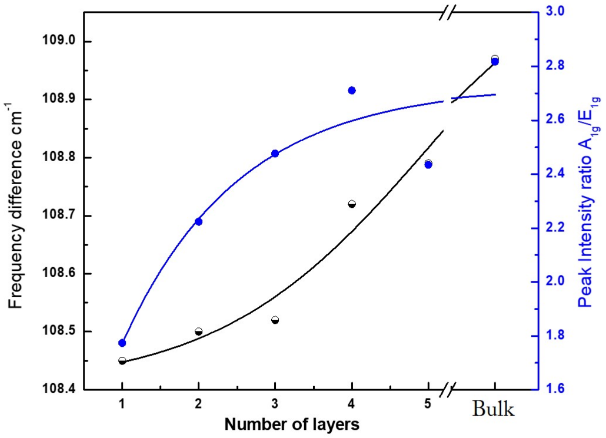

Figure 2.13: The frequency disparity (black curve) and the peak intensity ratio (blue curve) between A1g and E1g vibrational modes are plotted as a function of the SnS_2 layer thickness.

For slabs composed of four or more layers, $\Delta\omega$ converges to the bulk value at around 108.7 cm-1. Distinctly, from Bulk to monolayer the A_{1g} peak exponentially increases in intensity, proving that the ratio of the intensity of both modes could also provide proof of representing sample thickness.

SnS_2 was also characterized by high-resolution TEM (TS-Talos F200X) at McGill's Facility for Electron Microscopy Research (FEMR). Figure 2.14 shows a High-Resolution (HR) TEM image of a home-prepared SnS_2 sample under low magnification, where a continuous, high-quality layered structure can be observed. The image indicates the clear atomic chains both in a [100] and a [010] directions. The inset image with white lines indicates our sample's lattice spacing of 0.316 nm which is assigned to the (100) plane, is consistent with the hexagonal lattice. Blue and yellow balls indicate the presence of Sn and S atoms, respectively. Figure. 2.15 confirms the good crystallinity and high purity of the prepared SnS_2. The intensity of the higher order of Bragg's peaks

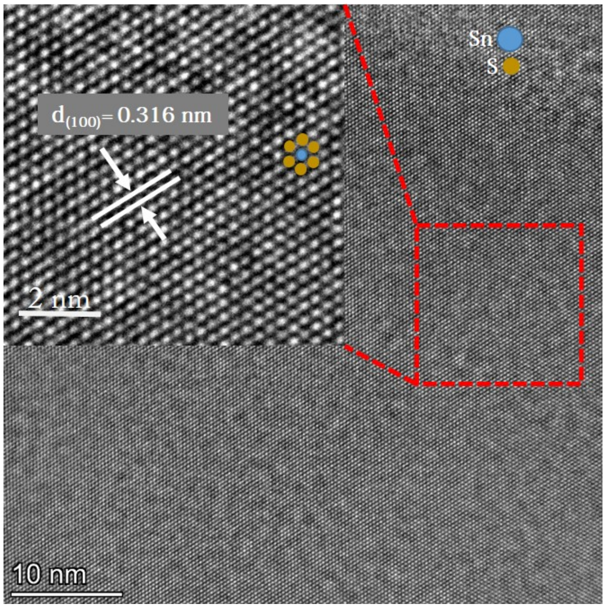

Figure 2.14: HRTEM (High-Resolution Transmission Electron Microscopic) image of bi-layered thick SnS_2 prepared with metal-assisted tape exfoliated at CPM.

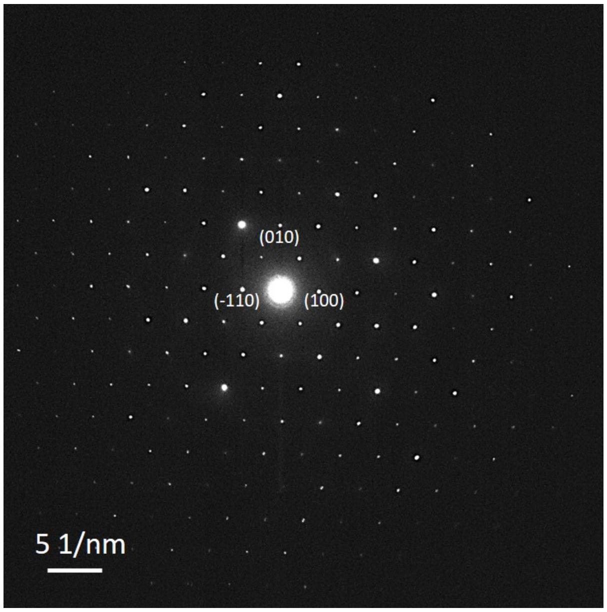

Figure 2.15: Selected Area Electron Diffraction (SEAD) of SnS_2 layer.

remains consistent over a large area of diffraction image. This characterization analysis is later compared by simulated Multislice calculations of diffraction patterns for SnS_2 (monolayer, 3x3)-crystal. Figure. 2.16 (A) depicts a HRTEM simulated image of 3x3 unit cell SnS_2 monolayer, and (B) inset images represents the Electron diffraction pattren of same unit cell. Different reflections, including zero and 2nd-order Laue zones, can be found identical by comprising our experimental images. The accuracy was achieved by considering correct parameterizations for accurate electron diffraction analysis. Increasing the cell size in multislice simulations can lead to difficulties in obtaining accurate results because it relies on discretizing the crystal structure into smaller cells. As the cell size increases, the level of discretization becomes coarser, which can lead to the loss of fine details in the simulated TEM images. In result larger cell sizes may cause blurring or distortion of atomic positions, resulting in inaccurate high-resolution images.

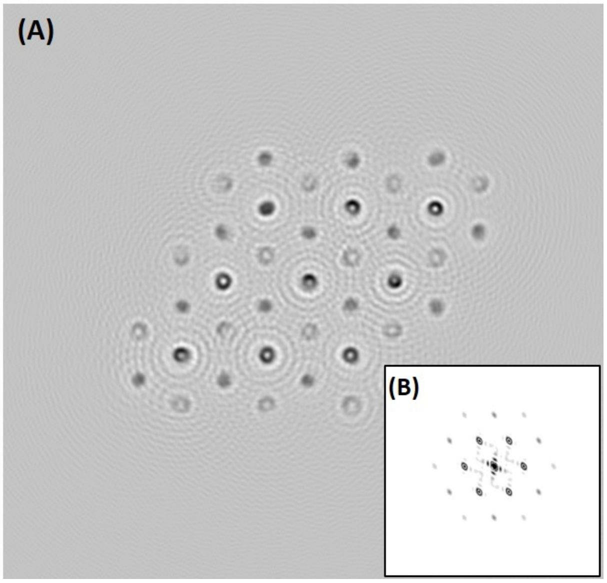

Figure 2.16: Multislice simulated images of SnS_2. (A) HRTEM image of 3x3 unit cell (B) Electron Diffraction of same unit cell.

2.2.4 Implementation on superconductor $Bi_2Sr_2CaCu_2O_8$

To prove the adaptability of this Au-assisted tape exfoliation technique in Siwick Lab, I took the challenge to test it on a bulk $Bi_2Sr_2CaCu_2O_8$ (Bi-2212) single crystal high-temperature superconductor. Notably, the weak van der Waals-like coupling between the layers, facilitates cleaving or exfoliation, but material breaks as we thin down to achieve nanometer thickness. Structurally, this two-layer compound is composed of a rock-salt SrO-BiO-SrO charge reservoir layer stacked with two CuO_2-Ca-CuO_2 layers as shown in the Figure 2.17. Potential mapping was done by using multislice simulations which indicates that oxygen impurities in Bi-2212 can occupy at least two distinct sites. Recently, optimally doped Bi-2212 exhibit superconducting fluctuations above the critical transition temperature (T_c= 97K), and the effect of thermal disorder on phase coherence can be countered by mid-infrared pulse excitation [40]. We received UD-60 (Under Doped) Bi-2212, where the concentration of charge carriers is lower than the optimal level, lowering the superconducting transition temperature (T_c = 60K) due to a strong propensity for charge-ordering. We are planning to conduct the UES experiment to observe the charge ordering in UD Bi-2212 cuprate superconductors. Charge ordering involves the spatial modulation of charge density, which can

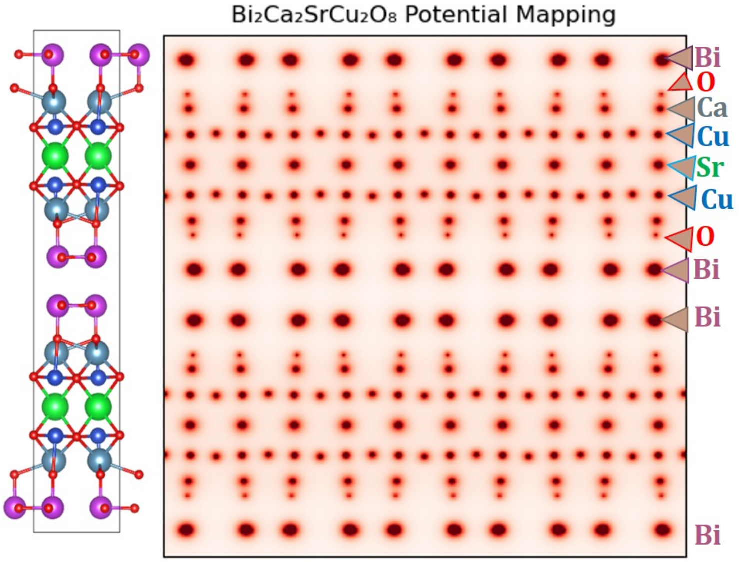

Figure 2.17: Potential mapping of Bi-2212, where each color pointer represents the element name in the map which is comparable to structural schematic adjusted in parallel.

lead to the distortion of the crystal lattice. This spatial modulation, hence, results in the forming of Cooper pairs, which is responsible for superconductivity. However, it is also possible that charge-ordering can disrupt the electronic states required for Cooper pairs to form and move freely, thereby suppressing the superconducting state. Temperature, doping concentrations, and the strength of the interactions between the electrons and the lattice vibrations (phonons) all have an impact on how these two phenomena interact with one another. This complex interplay can be understood by conducting UES experiments in Siwick lab; therefore, achieving an ideal UES sample preparation could be vital for comprehending the structural basis of the property in question.

The structure, oxygen content, and phase diagrams of High-Temperature Superconductors (HTSC) have all been extensively studied using Raman spectroscopy, particularly in bulk Bi-2212 single crystals [41]. The thickness dependency of the spectra in two distinct wavenumber ranges 1000-3000 cm^{-1} and 50-800 cm^{-1} was investigated using Raman spectroscopy techniques [42, 41]. These parameters were selected to investigate the material's phonon frequencies and vibrational modes. Their findings showed a distinct relationship between the detected Raman spectra in these locations and the sample thickness. However, it should be noted that the samples under investigation were prepared and reported on silicon wafers. For characterization, like TEM or ul-

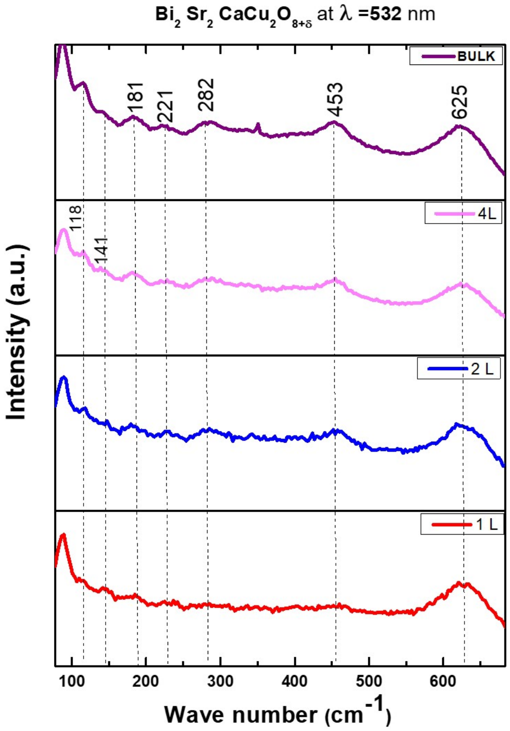

Figure 2.18: Multiple Raman spectras from single layer to bulk $Bi_2Sr_2CaCu_2O_8$ in the spectrum range of 100 to 660 cm^{-1}.

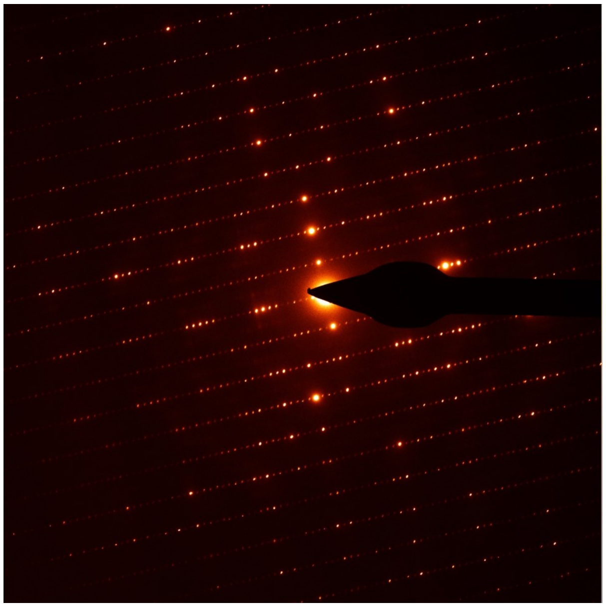

Figure 2.19: Selected Area Electron Diffraction (SAED) of Au-tape assisted prepared single crystal 4-layered $Bi_2Sr_2CaCu_2O_8$ sample.

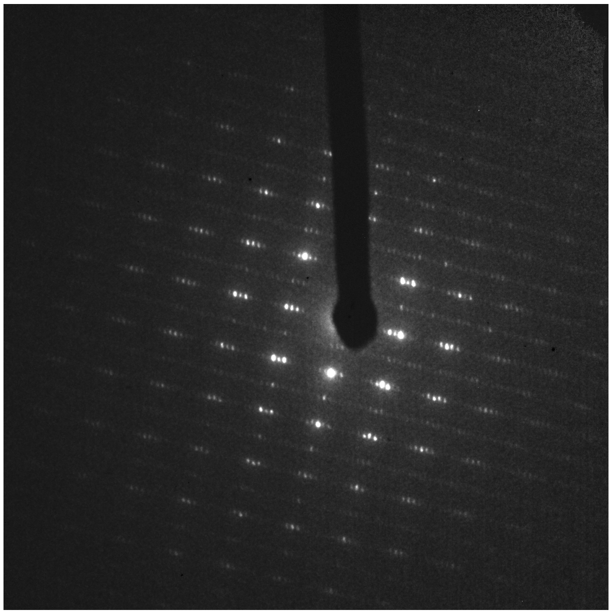

Figure 2.20: Few-layers thick $Bi_2Sr_2CaCu_2O_8$ electron diffraction image taken on UES instrument at Siwick lab McGill.

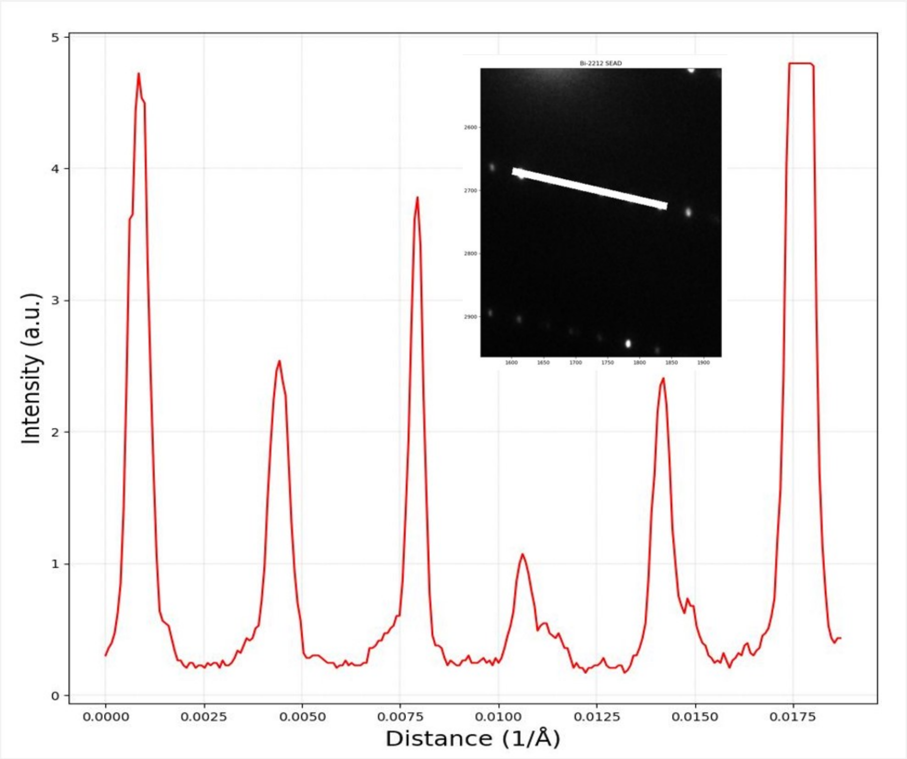

Figure 2.21: A line cut plot of Bi-2212 representing six diffraction peak intensities in reciprocal space.

trafast electron diffraction (UED) investigations, the usage of silicon wafers as substrates has been a restriction. Moreover, inaccuracies in the data can occur from the silicon substrate's introduction of background signals and interference with the Raman measurements. As a result, the interpretation of the sample's vibrational properties can be impacted by the substrate's impact on the Raman signals.

Figure. 2.18 shows a Bi-2212 sample micro-Raman spectra, gathered using a 532-nm excitation source. The spot size (of laser) is approximately 2μm, which is 10x smaller than our sample size (200μm), ensuring reliable spectral data for the samples with various thicknesses. During the measurement, I noticed that the few-layered Bi-2212 single crystals sample cannot sustain and burn by laser radiation (5 mW) as the laser will penetrate through the layers and most of the heat is accumulated by the layers. Due to the low thermal conductivity of the Bi-2212, therefore, after optimization, we adopted a laser power of 3 mW and an exposure time of 20 sec to avoid possible damage while keeping reasonable output intensity. To increase the signal-to-noise ratio, the data were aggregated five times. There was no cooling time allowed throughout the measurement. In bulk curve (Figure 2.18), Seven peaks around 118, 141, 181, 221, 282, 453 and 625 cm^{-1} were recorded. No other peaks were recorded higher then 700 cm^{-1}. The peaks around 118 and 626 cm^{-1} can be assigned to A$_1g$-symmetry vibration of the heavy Bi atom and the A$_1g$-symmetry vibration of Sr along the c-axis, respectively. The peak at 453 cm^{-1} is assigned to the O vibration and 282 cm^{-1} line has often been associate to the O$_{Cu}$ B$_1g$ mode. Raman peaks below 100 cm^{-1} should not be considered, because its due to an interference filter placed in the direction of incoming light. As the thickness of our crystal decreases, the peaks become weaker. Due to the material's constricted dimensions, phonons (vibrational modes) can be contained within thin films or layered structures. As the sample's thickness is reduced, this confinement effect may result in a low density of phonon states, which would attenuate the Raman scattering intensity. Figure. 2.19 represents a SAED of a home-exfoliated Bi-2212 sample from TS Talos F200X TEM. This image defines the remarkable quality of our samples. Figure. 2.20 represents the electron diffraction image taken in Siwick lab with an Ultrafast electron scattering setup. Figure. 2.21 shows a slice of a SEAD Bi-2212 line cut plot along the c-axis of diffraction peaks. To determine the lattice spacing along the (inset white) line cut (Fig. 2.21), the pixel spacing was known (0.000763619 / Å); from this, we can calculate the reciprocal distance by measuring pixel distances from the center and multiplying by the reciprocal pixel spacing. The lattice spacing along c-axis is found to be 5.7nm as the sample is under-doped. The existence of a 4x1 incommensurate superlattice explains this clusters of peaks seen in the electron diffraction image of Bi-2212. The arrangement of atoms and their interactions give rise to this superlattice structure, which changes the electron density and atomic positions in particular directions. When the material is exposed to electron beams, this configuration generates alternating zones of higher and lower electron density, resulting in variations in the diffraction pattern. The electron diffraction image shows these variances as peaks in clusters. Regarding the concept of the 4x1 superlattice, it involves a periodic pattern that is more subtle than distinct lines running through the material. Instead, it's a modulation of the atomic arrangement along one direction, which results in a distinct diffraction pattern due to the interference of electron waves.

The absence of explicit lines in the 4x1 reconstruction observed in our samples might be attributed to either defects, such as oxygen vacancies, or to the physical state of the sample, such as wrinkles. Oxygen vacancies can disrupt the periodicity, leading to a less defined superlattice structure in the diffraction pattern. Similarly, wrinkles in the sample can distort the superlattice, causing irregularities in the diffraction pattern that obscure the clear lines typical of a well-defined 4x1 reconstruction. These wrinkles could be a result of stresses induced during sample preparation or handling. Therefore, both defects and physical deformations need to be considered when interpreting the observed diffraction patterns, as they play a significant role in the manifestation of the superlattice's nature, which is intricately linked to the electronic interactions and lattice vibrations in the material.

2.3 Future Objectives

Through the utilization of our Au exfoliation technique, we are poised to embark on the investigation of two intriguing materials, namely $TiSe_2$ and $SnSe_2$, which have not yet undergone exfoliation using this method. Distinguished by distinct crystal structures from sulfides, these compounds exhibit diverse interaction strengths with the Au employed in our technique. It is noteworthy that the metal-to-layered material adhesion in the case of $TiSe_2$ and $SnSe_2$ is less robust. This facet sparks future interest and exploration, potentially yielding insights into novel phenomena such as "twistronics". This field delves into captivating phenomena like magic angles and Moiré landscapes observed in two-dimensional bilayers, enriching our understanding of layered material behavior and enabling innovative applications. Our endeavor to extend our methodology to these compounds presents an exciting avenue for uncovering new dimensions of material interactions and phenomena in the realm of two-dimensional materials.

Chapter Summary

This chapter successfully demonstrates a universal technique for the simple layer-by-layer disassembly of a vdW single crystal into monolayers of macroscopic dimensions. we put WS_2, Graphite, SnS_2, and $Bi_2Sr_2CaCu_2O_8$ under productive treatment of metal-assisted exfoliation and achieved monolayers results. The fabrication technique employed in our study, while meticulous and labor-intensive, resulted in a yield of approximately 60%. This figure reflects the rate of successfully prepared samples relative to the total number attempted. It is important to note that even after successful preparation, there is a susceptibility to sample breakage, which further underscores the delicate nature of the process. In the course of this study, a total of three samples of each type, as previously mentioned, were successfully fabricated. This quantity aligns with the objectives of our experimental design, allowing for sufficient replication to ensure the reliability of our results while contending with the practical limitations imposed by the intricate nature of the sample preparation method.

Chapter 3

VO_2 Composites: B, M and R Phase Exploration

We have learned how to achieve large dimensions mono- to few-layer single crystal thin films for our UES experiments with Au-tape assisted exfoliation this far. In this chapter, I will address and intercept the undesired Phase issue in VO_2 *polycrystalline thin films which were grown by pulsed laser deposition (PLD) technique. This chapter covers a systematical investigation results conducted by using Raman spectroscopy, on* VO_2*, which surprisingly led to the observation of an unusual and unexpected B-Phase that had not been previously seen in past PLD depositions. By plunging into our group's past experimental achievements on* VO_2*, B-phase is not the desired phase since we aim for the equilibrium stable M1 phase for our next experimental expectations. In order to get the perfect M-Phase, we shall go over how this enigma was solved.*

3.1 Fundamentals of Vanadium Dioxide (VO_2)

Vanadium dioxide (VO_2) is an n-type semiconductor with a band gap of 0.5-0.7 eV at room temperature. Its low symmetry Monoclinic (P21/c-space group) structure is known to be the equilibrium stable (low-temperature) phase. Interestingly, the material possesses a rutile (P42/mnm-space group) structure at temperatures above 340K. This structural phase transition is associated with an

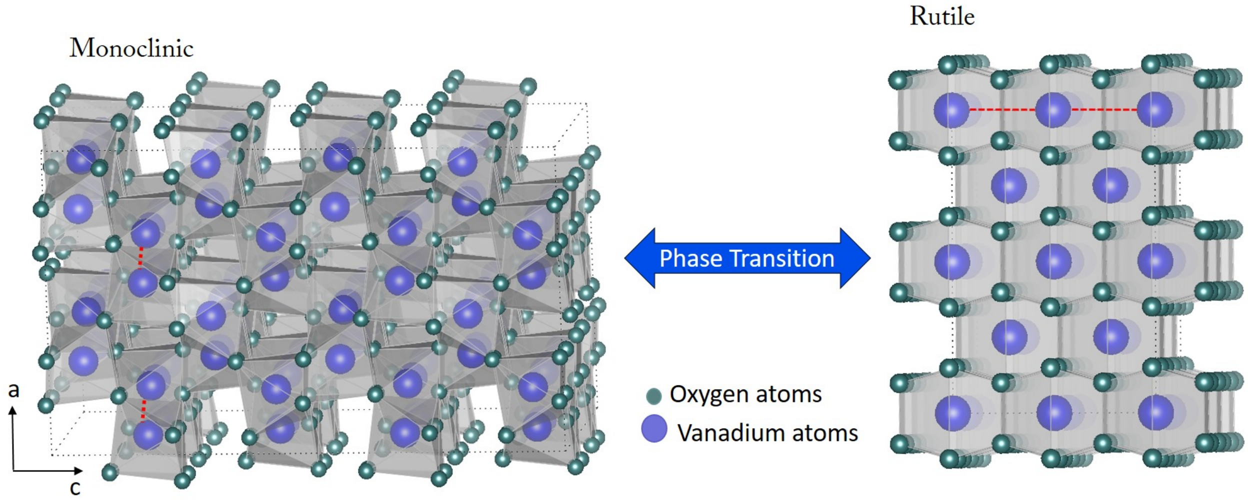

Figure 3.1: A Schematic showing structural phase transition from Monoclinic VO_2 where V-V dimers are evident along a-axis of the material, but absent in Rutile phase of VO_2 under equilibrium conditions. This structural transformation is associated with an insulator-to-metal transition that changes the resistivity by $\sim$6 orders of magnitude in pure samples.

insulator-to-metal transition (IMT) in electronic properties that has been extremely well studied but only recently somewhat understood. The remarkable complexity and richness of the IMT in VO_2 has made it one of the benchmark problems in condensed matter physics. Monoclinic lattice constants are a = 0.575 nm, b = 0.452 nm, and c = 0.538 nm with cell angle $\beta = 166.22^o$, Similarly a = b = 0.455 nm and c = 0.286 nm are considered to be lattice parameters for Rutile phase in VO_2 [8]. In the Monoclinic phase, the Vanadium (V) atoms are located at the off-centered location of the octahedral interstitial site made by the oxygen (O) atoms, as represented in Figure 3.1 (Left). The octahedra within a given unit cell and those in adjacent unit cells share a mutual edge, each with distinct alternating V-V distances. The Rutile phase exhibits high structural symmetry, featuring vanadium atoms situated at the centers of regularly shared oxygen octahedra which makes a metallic Vanadium chain along the c-axis of the structure as shown in Figure 3.1 (Right). In Rutile the dimerization of the V atoms along the c-axis causes this structural phase transition and unit cell doubling. The detailed discussion of electronic band structure and phase transition in VO_2 will be deferred to Chapter 4.

3.1.1 VO_2 polymorphism

Monoclinic (M1) and Rutile (R) phases are stoichiometric VO_2 polymorphs. This indicates that the ratio of vanadium (V) to oxygen (O) atoms in their crystal formations is set and particular. Due to variation in Oxygen vacancies in VO_2, it exhibits a number of polymorphic forms, such as VO_2(M2), VO_2(M3), VO_2(A), VO_2(B) and VO_2(C) [43]. These polymorphs have a wide range of useful applications, including those for catalysts (M1), cathode materials for reversible lithium-ion batteries (B), gas sensors (B, M), optical switching devices (A, M) and intelligent thermochromic windows. VO_2(M) and (R) are the most extensively studied phases for their structural transitions. The metastable VO_2(B) polymorph was proposed to display the irreversible structural transition from an Insulator to Metal (IMT) above room temperature [44]. It's a monoclinic layered structure similar to V_6O_{13} with lattice parameters a=1.23 nm, b=0.369 nm, c=0.642 nm and β = 106.6^o [45]. It's reported electrical resistivity decreases over a broad range of temperatures (-123^oC to 127^oC).

3.2 Pulsed Laser Deposition grown VO_2 thin films

Thin films of pure VO_2 and its polymorphs have been synthesized using various methods, such as vacuum evaporation, molecular beam epitaxy, and magnetron sputtering. However, among these techniques, Pulsed Laser Deposition (PLD) stands out for its numerous advantages [46]. Among several, one big advantage of PLD is that it enables fine control of the deposition process, including control of the crystal structure, stoichiometry, and film thickness. The well-defined energy and duration of the pulsed laser enable precise and regulated material transport. Our research group set out on a thrilling trip to undertake unique time-resolved UES (ultrafast electron scattering) investigations on extremely high-quality grown VO_2 samples by utilizing the many benefits of PLD technique. These meticulously deposited VO_2 samples from INRS (Institut national de la recherche scientifique) had exceptional characteristics that suited our research in the past [17, 16, 47]. Our collaborators at INRS were able to modify the samples to meet the demands of our experimental setup. The precise control over film thickness, crystal structure, and stoichiometry provided by PLD allowed them to tailor the samples to our experimental needs. With the aid of this innovative method, my seniors probed the ultrafast dynamics involved in the laser-induced insulator-to-metal transition in VO_2, revealing detailed features of its phase transitions and electron-lattice interactions [8, 47]. During follow-up experiments in 2020, to probe the nature of electron-phonon coupling in the strongly correlated R-phase experiments that had not previously been performed on VO_2, I encountered some challenges with received VO_2 samples, Which will be addressed in the following section 3.2.2. First, let's shed the light on previously received PLD parameter grown VO_2 samples.

3.2.1 Optimal PLD conditions of past VO_2 samples

In the laboratory of Nanofabrication facility at INRS, high-quality stoichiometric polycrystalline vanadium dioxide films had previously been fabricated many times by means of PLD process. For this purpose a pure vanadium target (99.95%) was used with a KrF excimer laser (λ= 248 nm) in an oxygen ambiance with a pressure of 15 mTorr and substrate temperature of 500^{o}C. The samples was 70 nm thick and grown on 50 nm thick amorphous silicon nitride (Norcada) TEM windows. The sample area is formed by a 250 μm x 250 μm silicon nitride window size of the substrate.

3.2.2 Obstacles in utilizing PLD as-deposited VO_2 samples in 2020

In our pursuit of advancing pump-probed UES experiments on VO_2 samples to study critical electron-phonon interaction in the R-phase (for details, refer to Chapter 4), I acquired a batch of samples from INRS. These samples were supposed to be deposited using the same PLD parameters as mentioned in the section 3.2.1. The deposition was made on Silicon Nitride (Si:N) TEM substrate (Norcada), with 50 and 100 nm window layered thicknesses. VO_2 film thickness on those windows was kept at 50nm. However, despite their successful deposition, the samples presented notable challenges when utilized in our pump-probed UES experiment. The main issues are addressed below

- The stability of our investigations was hampered by the sample's susceptibility to damage at far lower pump fluences than were previously used in our experiments (up to 40 mJ/cm^2) during laser irradiation. It was never reported in past experiments.

- The polycrystalline nature of some samples led to very poor diffraction patterns, making it challenging to obtain precise structural information.

- We face uncertainties in precisely characterizing the phase of the received samples. Due to the small size of VO_2 samples, XRD analysis becomes impractical, and the poor UED patterns obtained were inconclusive as to whether the film was actually in the desired M1 phase.

We actively explored various approaches to characterize the deposited VO_2 films. First, we performed X-ray diffraction (XRD) analyses on VO_2 samples produced with identical PLD conditions but deposited on Silicon (Si) substrates, as discussed in section 3.3. Secondly, HRTEM and SAED analysis was conducted to test morphology, VO_2 crystal orientation, and examine its defects. Additionally, we execute advanced Raman spectroscopic techniques to probe the samples as a function of laser power, temperature, and background ambient conditions.

3.3 Structural analysis with X-Ray Diffraction (XRD)

In this section, we first investigate the structural quality of VO_2 thin films of 50nm and 100 nm thickness grown on Silicon (1 0 0) ultra-clean substrates via PLD, keeping the deposition parameters identical to the above-mentioned section 3.2.1. For this purpose, θ-2θ XRD diffraction patterns of films with thicknesses 50 nm and 100 nm were conducted, as shown in Figure 3.2. There are no noteworthy changes in the structure with thickness. Two main peaks appear at 2θ=27.8^o and 42.2^o. These angles correspond to the Bragg angle with (0 1 1) and (2 1 0) orientation of the VO_2 (M1) phase, respectively.

The films produced on the silicon substrate significantly display VO_2 M-phase properties, according to the X-ray diffraction (XRD) investigation. However, it is crucial to consider that film

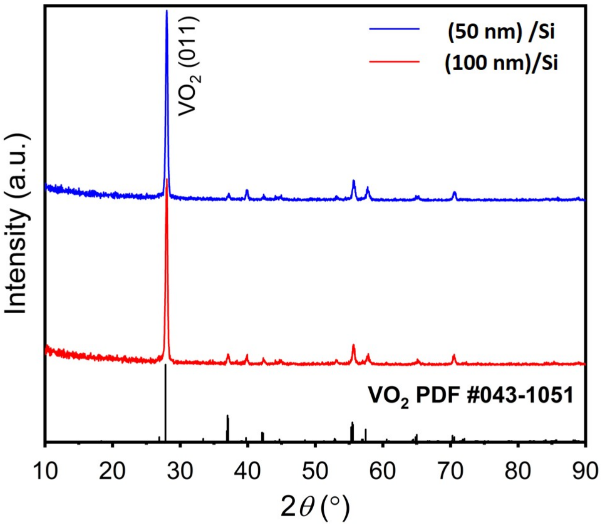

Figure 3.2: XRD spectra of VO_2 on Si substrates, blue spectrum represents 50 nm film thickness and red spectrum indicates 100 nm film thickness deposited via PLD, black lines represent the monoclinic-phase of VO_2 peak reference from the database (JCPDF Card No. 043-1051).

growth is intricately linked to the surface energy and morphology of the substrate (Si). It is more likely that the M-phase will come out on top because these films were produced on silicon, especially when compared to thin Si:N windows. The substrate choice plays a critical role in influencing the phase preferences during film deposition [45].

3.4 TEM and SAED analysis on VO_2

Our investigation into the issues we were experiencing with the VO_2 samples started with the support of TEM (Transmission Electron Microscope) analysis. TEM and SAED (Selected Area Electron Diffraction) analysis was conducted on 50 nm thick VO_2 film, deposited via PLD on 50 nm (Si:N) TEM window.

Figure 3.3(a) represents a TEM image of an as-received VO_2 film, that seems composed of numerous small crystalline grains with varying orientations, which can be attributed to several underlying factors. During PLD films growth, the critical size and orientation of the film nucleation depend on the driving force, i.e., the deposition rate and the substrate temperature. Below critical substrate temperature surface mobility of the adatom remains slow, and less nucleation takes place,

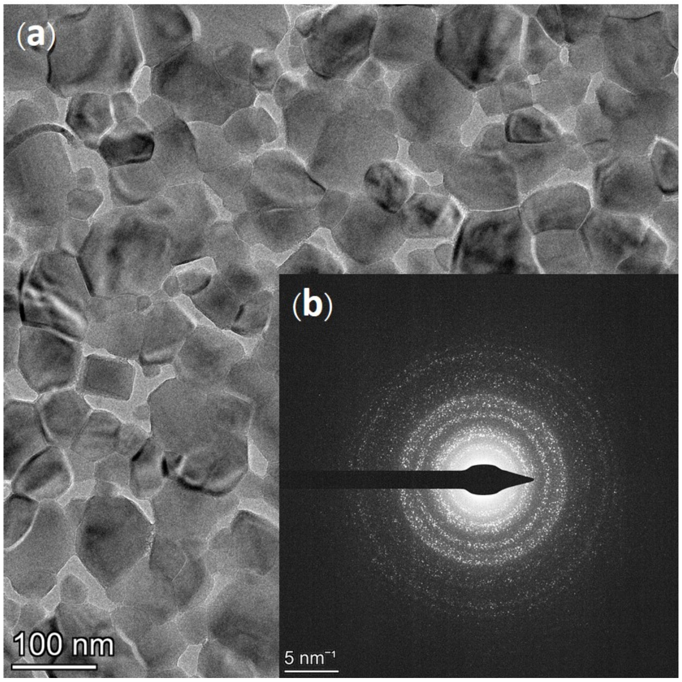

Figure 3.3: (a) Transmission electron microscopic image and (b) inset SAED (Selected Area Electron Diffraction) of a 50 nm thick polycrystalline VO_2 film, deposited via PLD on a 50 nm (Si:N) TEM substrate.

resulting in forming such small misoriented grains [48]. As shown inset Figure 3.3(b), SAED analysis indicates the presence of polycrystalline and nanocrystalline mix structures within the VO_2 thin films can often be detected by deformed granular diffraction rings. The lattice parameter was found to be a=1.21nm, b=0.39 nm, c=0.542 nm calculated from this SAED image indicated the presence of B-phase polymorph as mentioned in section (3.1.1). Furthermore, differences in the lattice orientation and crystallographic alignment within different regions of the thin film might be related to the occurrence of granular diffraction rings. The presence of such diffraction patterns is expected to result in any VO_2 polymorph that exhibits complex phase transitions and lattice distortions.

3.4.1 HAADF analysis on VO_2

A specialized, powerful complementary technique HAADF (High-Angle Annular Dark-Field) imaging, offers improved sensitivity to heavy elements and atomic number contrast. Character-

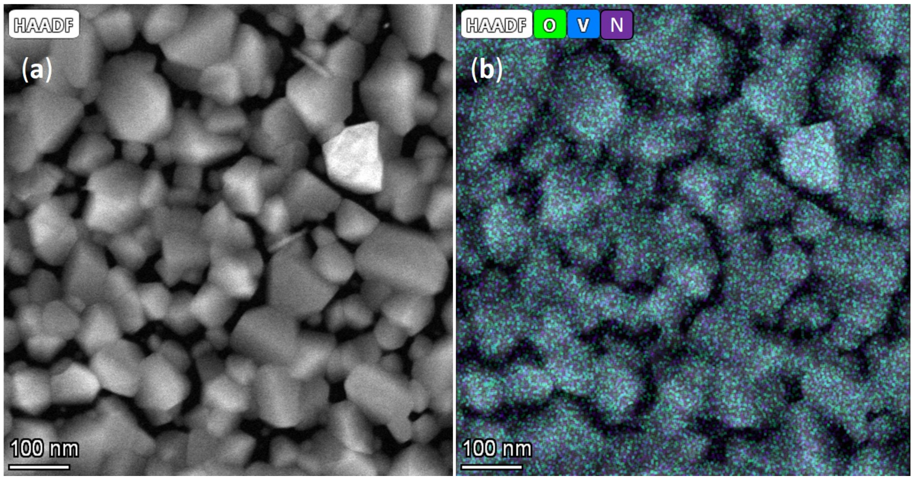

Figure 3.4: (a) HAADF-STEM image and (b) EDS (Energy Dispersive Spectroscopic) image analysis was conducted on a 50 nm thick VO_2 sample, deposited via PLD on a 50 nm (Si:N) TEM window/substrate.

izing nanoscale materials like thin films, nanoparticles, and interfaces makes use of it particularly well. In our study of the PLD-grown VO_2 thin film, the HAADF-STEM technique was instrumental in revealing the elemental composition. This was achieved through the technique's ability to differentiate elements based on their atomic numbers, creating a contrast in the image that correlates with the varying atomic numbers of the elements present As shown in Figure 3.4(a) regions with higher atomic numbers, such as vanadium-rich regions, would appear brighter, while oxygen-rich regions would appear darker. Image of an Energy Dispersive Spectroscopy in Scanning Transmission Electron Microscopy (EDS-STEM) is shown in Figure 3.4(b). This result provides us with the mapping of the elemental distribution in the film, which can help to reveal how uniformly the elements are distributed and how stoichiometry varies across the PLD grown VO_2 sample. Understanding the chemical heterogeneity, phase transitions, and compositional differences within the VO_2 thin film depends heavily on this information.

3.5 Raman characterization of VO_2

Recent developments in thin film synthesis provide fine control over stoichiometry, resulting in the production of metastable phases under nonequilibrium circumstances. The crystal phase must

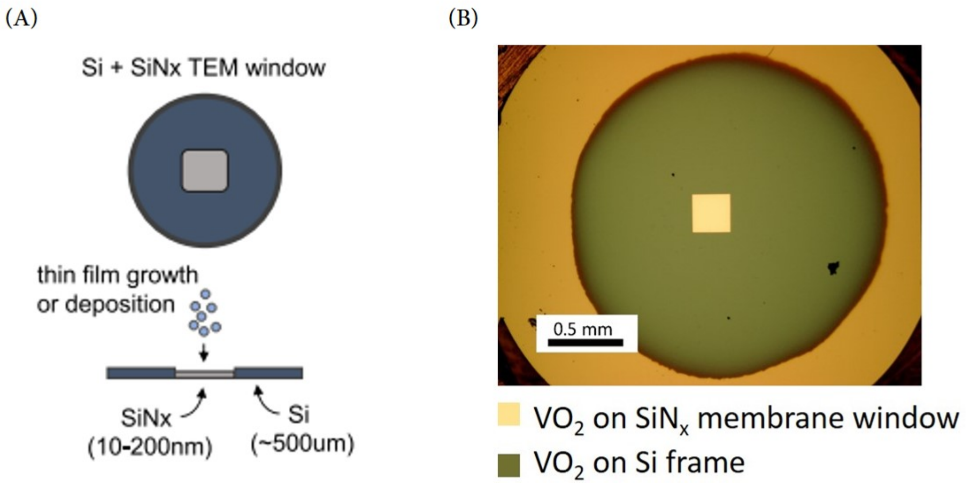

Figure 3.5: (A) Depicts the schematic of a single hole (Silicon: Nitride) Si:N layered TEM window/substrate, (B) An Optical microscopic image of VO_2 sample on Si:N TEM window/substrate.

be determined using a straightforward but efficient method. Raman spectroscopy rapidly delivers results on a millimeter scale without sample degradation. However, it requires reference spectra, which may not always be available. The opportunity to get around this restriction lies in creating trustworthy reference spectra and improving Raman spectroscopy as researchers investigate novel thin film materials and features. Fortunately, an in-depth analysis of 52 stable and metastable phases of the vanadium-oxygen system is available in the literature [43]. In our effort to identify the specific phases present in the PLD-induced VO_2 thin films, this priceless data is an essential tool.

3.5.1 B-Phase detection in VO_2

As mentioned above Raman measurements were demonstrated to further identify the phase information of VO_2 thin films. Figure 3.5 (A) shows a schematic of Si:N substrate, (B) shows an optical microscopic view of PLD grown VO_2 thin film sample substrate; The substrate is made of a Si (silicon) frame that is covered with 50 nm thick Si:N membrane. This Raman analysis was conducted on the substrate's distinct regions: the Si:N **frame** and the Si:N **membrane**, it is important to remind that we kept the same sample for all of above-mentioned characterizations 50 nm thick VO_2 film, deposited via PLD on 50 nm Si:N TEM window.

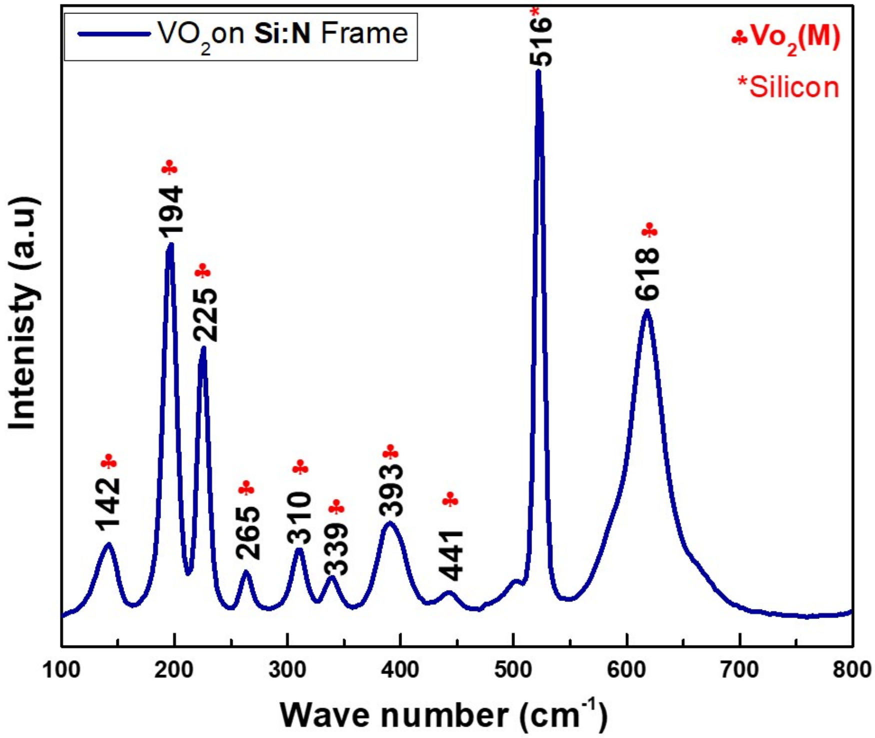

Figure 3.6: Raman spectra taken with 532 nm laser showing VO_2 (M1-Phase) on a 50 nm thick Si:N substrate **frame** deposited with PLD to the 50 nm thick film.

3.5.1.1 Raman on Si:N frame

Figure 3.6 presents Raman spectra of VO_2 thin films taken at room temperature on Si:N frame at 0.5mW laser power to avoid laser heating. This Raman spectra show a dominant VO_2(M1) phase since the observed peaks are found identical with the previously reported monoclinic (M1) phase [49]. I identified 9 peaks at wavenumbers 142, 194, 225, 265, 310, 339, 393, 441 and 618 cm^{-1}, which were in accurate agreement with reported VO_2(M1) phase [49, 50]. The observed Raman peaks were assigned as B_{1g}, A_g, A_g, A_g, A_g, A_g, A_g, E_g and A_g, respectively corresponding phonon modes [51]. Bending and stretching V-O-V bonds and zigzag chains of V-V are among the phonon modes of the monoclinic (M1) phase of VO_2 [50].

Three groups of vanadium-oxygen modes are used to categorize the VO_2 Raman spectra. The greater wavenumber bands ($>$ 800 cm^{-1}) are affiliated with V=O stretching modes of distorted octahedra and deformed square pyramids. Mainly interest are low wavenumber bands (400cm^{-1})

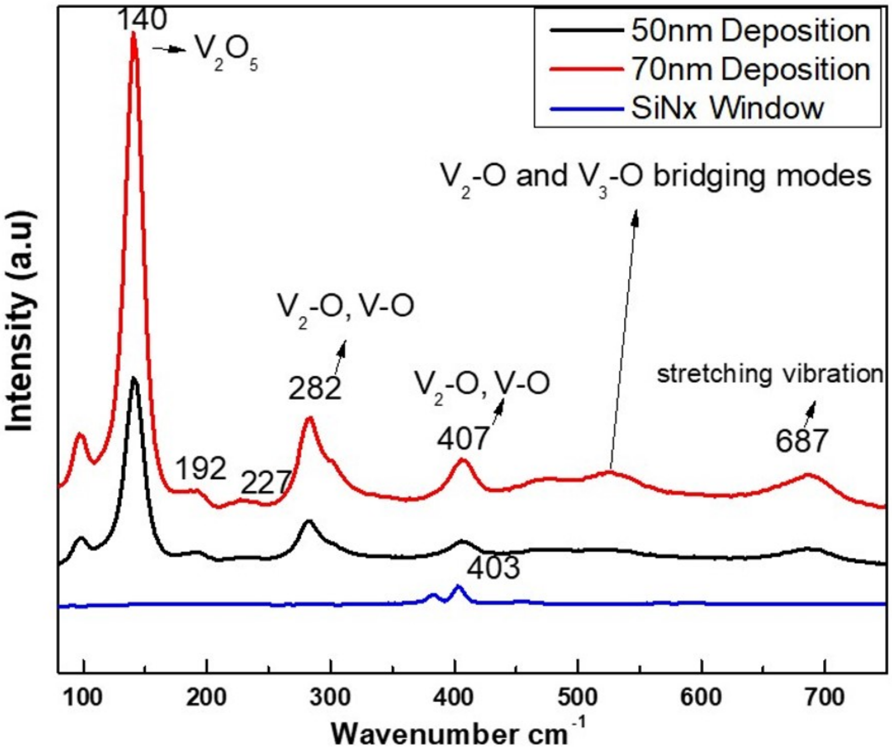

Figure 3.7: Raman spectra taken with 532 nm laser wavelength on 50 nm and 70 nm thick VO_2 samples indicating the presence of B-Phase on Si:N membrane deposited with PLD. Both thicknesses were deposited on a 50 nm thick **membrane**.

correspond's to V-O-V bending modes, the intermediate bands (400–800 cm^{-1}) to V-O–V stretching modes.

3.5.1.2 Raman on Si:N membrane

Figure 3.7 shows Raman spectra of VO_2 thin films taken at room temperature on Si:N **membrane** at 0.5mW laser power to avoid laser heating. Significant differences were observed between the obtained Raman spectra from this regions. Raman bands in Figure 3.7 a were characteristic of VO_2(B) Phase [52].

The membrane with VO_2 looks partially oxidized, which caused the band at 140 cm^{-1} to be caused by the lattice vibration of V_2O_5. Both the 282 cm^{-1} and 407 cm^{-1} laser bands may be attributed to the V_2O and V-O flexural modes, respectively. V_2O and V_3O bridging modes produced broadband with a wavelength of 400–600 cm^{-1}. V_2O stretching vibration was identified in the bands at 691 cm^{-1}, whereas V-O stretching mode often appeared near 1000 cm^{-1} [52].

Further, Raman analysis was carried out on different samples that had a layer of 70 nm thick deposition of VO_2 in order to further validate these results. Repeated tests consistently revealed that VO_2 was in its B-phase on the Si:N membrane and its M-phase on the Silicon frame. These findings highlight the critical role that substrate morphology/nature plays in determining the crystal phase of the deposited VO_2 thin films. The difference in Raman spectra between the Si:N frame and the Si:N membrane (as shown in Fig. 3.6 and 3.7 respectively) points to the possibility of various epitaxial effects and growth circumstances in each area of the substrate, as shown in TEM analysis as well. The significance of PLD parameters in customizing the desired crystal phase of VO_2 thin films for prospective applications is highlighted by these discoveries, which provide useful insights for the optimization of thin film growth processes.

3.6 New growth parameters of PLD for VO_2

After we contacted INRS, they provided us with an update on their modified PLD strategy. The substrate temperature was raised to 600°C, and the target-to-substrate distance was changed to 65mm, among other significant adjustments to the deposition parameters. A 50 nm thick polycrystalline VO_2 samples were prepared via PLD on 30, 50, 100 nm Si:N TEM substrate with 250 x 250 μm window dimensions. These adjustments were made, and the Monoclinic (M1) phase of VO_2 was successfully deposited on the chosen TEM Si:N window. Afterward, we conducted Raman analysis on the sample in order to verify the phase of the deposited VO_2, which amply demonstrated the M phase. After validating the phase identification, we successfully fixed the problem we had initially with VO_2. The following section will demonstrate our Raman analysis strategies to ensure about M-phase in VO_2.

3.6.1 VO_2(M) Phase confirmation at Room Temperature(RT)

In this section, VO_2(M1) Raman analysis was conducted in order to confirm the presence of M-phase. Figure 3.8 and 3.9 respectively represent Raman spectra conducted on Si:N frame and membrane individually. Three samples with varying Si:N thick membranes were used in the analysis, and all the samples agreed with the literature reported data on Monoclic M1 VO_2 Phase [50]. We notice that the VO_2 film with 50 nm thickness seems to provide better intensity spectrum, which reflects the good quality monoclinic phase deposited thin films. A slight blue shift in the peaks of 100 nm thick samples can be seen as well, which represents the small strain induced by the substrate surface energy.

3.6.2 Monoclinic to Rutile Phase Transition in VO_2 at Room Temparature

The Figure 3.10 shows the Raman spectra acquired from a 50 nm VO_2 thin film under varying laser power in air ambiance. All of our measurements were conducted on by using 532 nm wavelength laser system, with power increments ranging from 0.1 mW to 1.30 mW. The observed Raman spectrum, or VO_2(M1), is noteworthy because it matches the VO_2 in the monoclinic phase. The material does, however, clearly switch to the Rutile phase of VO_2 when the laser intensity is increased to 0.75 mW. The generated laser heating on the Si:N membrane is responsible for this fascinating behavior.

The substrate experiences a localized increase in temperature as a result of the increased laser power, which facilitates the transformation of the VO_2 phase. The importance of managing laser power during Raman measurements is highlighted by the phase transition that was detected because it directly affects the material's structural behaviour. We can effectively investigate the dynamic phase transitions and responses of VO_2 thin films to external stimuli by meticulously controlling laser parameters and assuring precise temperature control, facilitating a deeper understanding of their intriguing properties and potential applications in advanced materials and devices.

Continuing our experiment with small increases in laser power, we found that the B-phase emerged in the Raman spectra of the VO_2 thin film with a further rise to 1.30 mWatt. This fascinat-

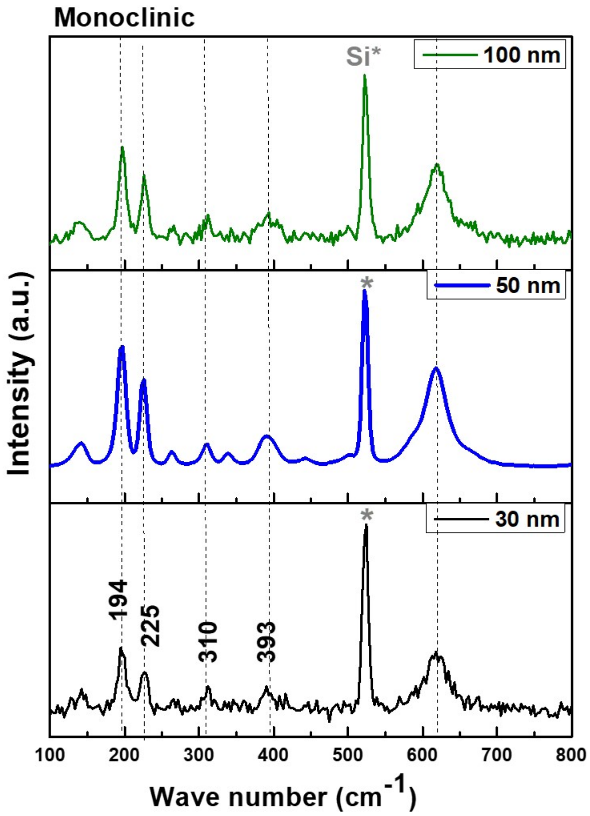

Figure 3.8: Raman spectra of M-Phase in VO_2 detected on 30nm, 50nm, and 100nm thick Si:N frame which was deposited with new PLD parameters. The thickness of each film after deposition was 50nm.

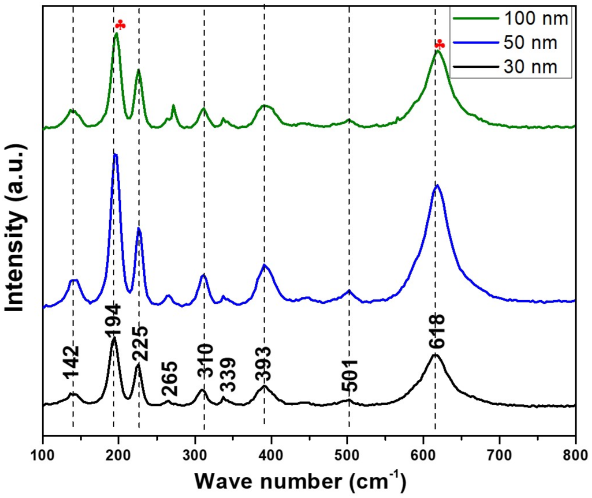

Figure 3.9: Raman spectra of M-Phase in VO_2 detected on 30nm, 50nm, and 100nm thick Si:N membrane deposited with new PLD parameter, The thickness of each film after deposition was 50nm.

ing finding offers important new information about the material's laser-induced phase transitions. Notably, optoelectronics and smart windows could both benefit from the B phase of VO_2 because to its distinct structural characteristics. The importance of this experimental strategy in revealing the complex behavior of VO_2 thin films is highlighted by the ability to trigger and regulate such phase transitions by precise laser power adjustments. The seamless transitions between the Monoclinic (VO_2(M1)), Rutile (VO_2(R)), and to B phase states now possible in our experimental system puts us in a good position to investigate the complex dynamics and functional features of VO_2 materials under various external stimuli like pump-probe experiment in our lab. This thorough analysis not only improves our understanding of the complicated phase behavior in VO_2 but also

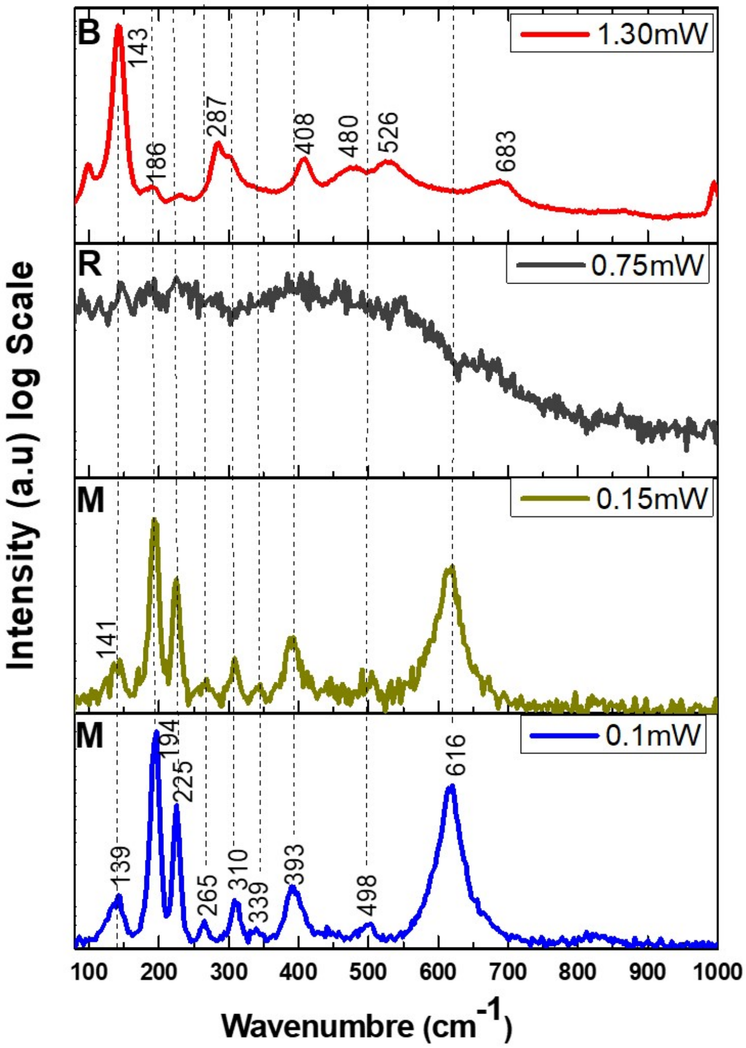

Figure 3.10: VO_2 Phase Transition at Room temperature from Monoclinic to Rutile phase and Rutile to B - phase concerning laser-induced heating by varying laser power in air ambient.

shows how sensitive the phase is to PLD deposition conditions. This will create opportunities for new materials and gadgets with specialised functions for various technological uses.

3.6.3 Temperature dependent Raman Hysteresis VO_2

Three different samples with substrate membrane thicknesses of 30, 50, and 100 nm were examined using temperature-dependent Raman analysis to determine the effect of Si:N membrane thickness on the phase transition temperature of VO_2. The phase transition behavior from mono-

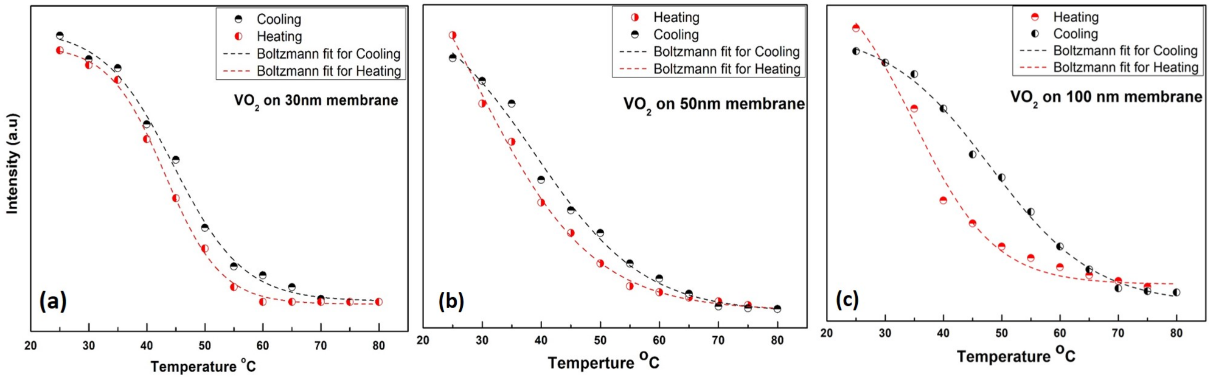

Figure 3.11: Temperature-dependent Raman hysteresis of VO_2 thin film grown on (a) 30nm (b) 50nm and (c) 100nm thick Si:N TEM window substrates

clinic VO_2(M1) to rutile VO_2(R) was studied and Figures a, b, and c show the associated transition temperatures.

Figure 3.11a shows the phase transition temperature to be at ∼52°C, while Figure 3.11b shows it to be around ∼55°C. Another phase transition temperature was seen in Figure 3.11c, which was around ∼53°C. It's interesting to note that all three transition temperatures were discovered to be slightly lower than the reported phase transition temperature for VO_2, which is 68°C. The difference in phase transition temperatures is caused by the thickness of the Si:N membrane, which has an impact on the thermal stability and confinement effects that the VO_2 thin films encounter. Si:N membranes that are thinner, Are known to have improved thermal conductivity, allowing for effective heat dissipation from the VO_2 layer. As a consequence, the temperature gradients across the membrane may become more pronounced, resulting in a shift towards lower transition temperatures due to reduced thermal confinement. PLD parameters could also effect the transition temperature of the thin films. The altered phase transition temperature may also be influenced by the epitaxial strain inherited by the Si:N membrane. The structural stability and phase transition behavior of VO_2 may change as a result of induced strain effects brought on by the lattice mismatch between VO_2 and Si:N.

Chapter Summary

In pursuit of time and momentum-resolved UES experiments on VO_2, we encountered many problems with the set of PLD grown VO_2 thin film samples obtained from our INRS-EMT collaborators in 2020. Our Raman analysis and TEM analysis of VO_2 samples revealed an unanticipated problem: The film deposition over TEM windows were not in the equilibrium stable M1-phase. Furthermore, the Raman analysis did not match what we had anticipated. After further investigation, we obtained an unusual finding: only in the Si:N substrate window area, where the silicon (Si) was thinner, the Raman spectra indicated the presence of the B-phase of VO_2. This discovery raised a significant concern as the expected phase should have been the Monoclinic (M) phase, not the B-phase.

The presence of the B-phase instead of the Monoclinic phase in specific regions suggests that localized factors during the film growth might be influencing the phase stability of VO_2. One potential explanation could be the temperature variations during the deposition process. Given that VO_2 exhibits a phase transition highly sensitive to temperature, any uneven temperature distribution across the substrate during growth could lead to the formation of different phases. Another possibility is the strain induced by differences in the thermal expansion coefficients between the VO_2 film and the Si:N substrate. Thinner silicon areas might be more susceptible to strain effects, which can alter the crystal structure and phase of VO_2. This strain could be sufficient to stabilize the B-phase, which is not typically favored under standard growth conditions. Therefore, a detailed investigation into the thermal and mechanical properties during the film deposition process is essential to understand the formation of the B-phase in these localized areas.

We contacted our INRS collaborators in an effort to find a solution to this problem, and they let us know that their Pulsed Laser Deposition (PLD) method had recently changed. We advised them to go back to the earlier technique they used since we could see the possible effects of this move. They implemented the original PLD parameters, to our delight, we were able to successfully get the Monoclinic phase (M1) of VO_2 on the window section. This discovery was crucial since it not only fixed the Raman data mismatch but also made it possible for us to move forward with R-phase Debye-Waller studies with UES.

Our future studies on the rutile phase is anticipated to provide further light on the fascinating characteristics and phase dynamics of VO_2 thin films, opening the door for innovative new advancements in functional materials and possible uses in cutting-edge technologies.

Chapter 4

Future Work and Outlook

A brief review of earlier and more recent theoretical and experimental research on phase transition stimulants in VO_2 *will open the chapter. These examples serve as crucial points of comparison and provide a solid foundation for placing our current findings in context. In the section that follows, we will switch our attention to an extensive empirical investigation and interpretative review of electron diffraction intensities that display temperature-dependent variations on carefully characterized* VO_2 *thin film. The goal was to clarify the complex mechanisms underpinning the material's dynamic responses to a range of thermal conditions. In the final section, we will outline our goals for next Deby Waller experiments on* VO_2*. Our focus is on exploring the enigmatic Rutile phase of* VO_2 *using an upgraded UES system.*

4.1 Contemporary picture of VO_2: Peierels or Mott metal-insulator transition?

Even after years of intensive study into the phase transitions of VO_2, the subject is still actively evolving and seeing substantial breakthroughs. The origin of the insulator-to-metal transition is the subject of two opposing theories. One theory projects the idea that monoclinic lattice distortion directly causes the transition to insulating electrical properties, while other emphasize that strong electronic correlations leads to electron localization and insulating behaviour. According to the first theory, put forth by Goodenough [53] in 1971, the lattice distortions that cause a band gap in the monoclinic M1 phase can be seen as occurring through a Peierls type mechanism. The second theory, advanced by A. Zylbersztejn and Mott [54] in 1975, asserts that an insulator-metal transition is observed on by strong electronic correlations, or more specifically, by the conflict between localised and delocalized electrons when the carriers are subject to strong inter-site (Vanadium -Vanadium) coulomb interactions. The contemporary understanding of the $\mathrm{VO_2}$ phases is significantly more complex. Powerful computational approaches like Dynamical Mean Field Theory (DMFT) and sophisticated experimental tools are still trying to interpret the relative importance of electron-lattice interactions and electron-electron interactions in the phase transition, which is still up for debate, but seem to point to the involvement of both Peierels type and Mott-Hubbbard type processes.

4.1.1 $\mathrm{VO_2}$ Band Structure

Before we dive deeper into the theoretical and experimental discussion, a basic understanding of $\mathrm{VO_2}$ band structure is extremely crucial to develop. Vanadium (V) atoms are commonly thought of in this context as having a $3d^1$ electronic configuration, which denotes the existence of a single electron in the valence $3d$ orbital shell. In the high-symmetry rutile phase, the vanadium atoms assume a central position within coordinated $\mathrm{VO_6}$ octahedra (refer to Figure 4.1 (a)). The five V-3d orbitals divide into separate states that exhibit e_g and t_2g symmetries by the intrinsic crystal field resulting from surrounding oxygen (O) atoms. The hybridization phenomenon between V-3d and O-2p orbitals results in the emergence of σ and π type orbitals (refer to Figure 4.1 (b)). A pronounced overlap is observed within the σ and σ^* orbitals (with the $*$ signifying anti-bonding), thus inducing a notably discernible energy splitting. This manifold technically causes the formation of two overlapping bands, which is named as $d_\parallel$ and π^*. The metallic conductivity of the R phase is carried by both of these bands. Moreover, structural distortions strongly influences the band structure of the material which leads to lifting of degeneracies and causing splitting of overlapped $d_\parallel$ and π^* band in M1 phase (as shown in Figure 4.1(b) right).

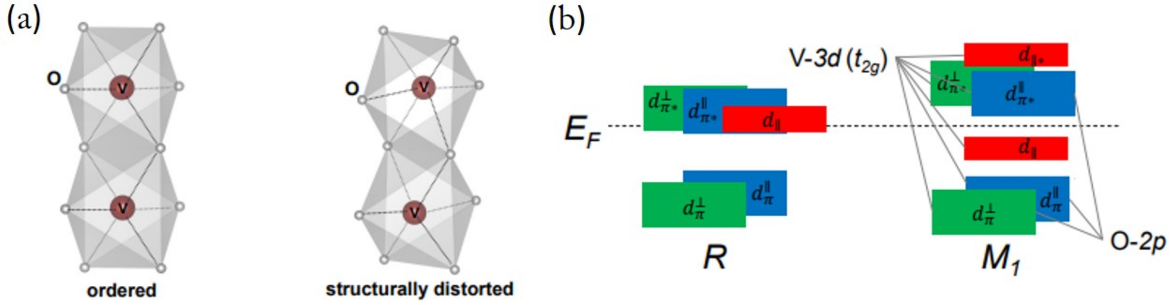

Figure 4.1: (a) Schematic of V-V pairs in Rutile (ordered) and Monoclinic phase (distorted), where each V atom is surrounded by 6 Oxygen atoms in R Phase and off-center Oxygen cage octahedra in the M1 phase (b) Corresponding Electronic bands of Rutile (left) and M1-monoclinic (right). This figure is adopted and modified from Martin's thesis [4]

4.1.2 Previous Theoretical and Experimental picture of VO_2

VO_2 displays structural simplicity with a small unit cell and a relatively high degree of symmetry throughout all phases. These qualities make VO_2 an excellent platform for computational and experimental studies, some of which are briefly discussed in this section.

4.1.2.1 Previous Theoretical perspective of VO_2

Eyert [55] used the local density approximation (LDA) and density-functional theory (DFT) to investigate the phase transitions between rutile, monoclinic M1, and monoclinic M2 VO2. Intriguingly, unless the lattice distortions are artificially increased to the point where the $d_{||}$ and orbitals do not overlap, this specific technique fails to produce a band gap for the M1 and M2 phases.

To examine the impact of electronic correlations in the M1 phase of VO2, Biermann et al. [56] combined dynamical mean-field theory (DMFT) and density functional theory (DFT). They described the M1 phase as insulating with a band gap of 0.6 eV through their simulations. They predict that the two d-orbital electrons of vanadium dimers create singlet states, which lead to the establishment of the insulating gap. The findings of the study by Biermann et al. point to the critical role that electronic correlations play in the downward renormalization of the split $d_{||}$ band energy and the subsequent opening of the band gap.

On huge supercells with hundreds of atoms, Weber et al. undertook a thorough research by combining cellular cluster dynamical mean-field theory (DMFT) and density functional theory (DFT) [57]. Their method used an iterative procedure that permitted modifications in the electron occupancy of the V-3d and O-2p states. An unexpected insulating state was discovered in the study, which was described as a "orbital selective Mott transition, assisted by the Peierls distortion", where bonds between the d_{xy} and d_{xz} states formed along C_R, each accommodating one electron, leading in a total occupancy of two electrons in the d states. This caused a Mott instability to appear in these states. The authors also looked into experimental data that supports this kind of orbital selective transition, which is crucial to our understanding of our future experiments.

The insulator-metal transition (IMT) in VO_2 is predominantly driven by electron-electron correlations (Mott transition), together with high intersite exchange correlations between dimers, according to recent studies by Brito et al.[58]. It should be noted that structural distortion is very important for promoting and strengthening correlation effects. The research shows that a Peierls-like transition in the adiabatic limit is connected to these intersite exchange correlations. In addition, they give estimates based on time-resolved IMT measurements that demonstrate the temperature dependence of the optical gap in VO_2. Surprisingly, given adequate interaction strengths, the suppression of correlation effects alone can cause the gap to close. Our grasp of the complex nature of the relationships between correlations and structural alterations is advanced by this integrated understanding of the phase transition in VO_2

4.1.2.2 Experimental (photo-excitation) perspective of VO_2

The transition between the insulating and metallic phases of VO_2 can be induced by photoexcitation using ultrafast laser pulses. Notably, the finding that, with enough fluence, the insulator-metal transition (IMT) may be rapidly initiated after femtosecond laser stimulation has opened up new research directions for exploring the kinetics of this fascinating phase transition. The material is successfully injected with energy by the ultrafast laser pulses, which encourage electronic excitations that cause VO_2 to quickly and irreversibly switch states at fluences lower than that required to photothermally drive the phase transition. The IMT in VO_2 may be better-understood thanks to this phenomena, which also presents interesting prospects for applications in ultrafast optoelectronic devices [47].

The first studies on the ultrafast kinetics of the insulator-metal transition (IMT) in VO_2 were carried out by Becker et al [59]. using laser excitation. They used 780 nm laser light and optical transmission and reflection techniques to evaluate the complicated index of refraction of a polycrystalline VO_2 layer. According to the results, the IMT happened at fluences more than 3.7 mJ/cm^2 during an ultrafast timescale of roughly 500 fs. Their findings revealed two unique timeframes, which prompted the creation of an updated electron plasma model with electronic properties that differed from the equilibrium metal state. The complicated ultrafast dynamics of the IMT in VO_2 were clarified by this novel method, opening the door to further investigation and possible optoelectronic uses.

Time-resolved X-ray diffraction studies on the photo-induced M1 to R phase transition in VO_2 by Cavalleri et al [60] were important. According to their research, the structural change happened quickly within 300 fs and displayed a nonthermal character above a threshold fluence of 7 mJ/cm^2. The transition is completely driven by electronic excitation and occurs at a pace that is faster than predicted by equilibrium electron-phonon coupling, according to this non-thermal behaviour. Additionally, they showed that the crystal phase transition (CPT) and the insulator-metal transition (IMT) appear to be simultaneous events. These findings enhanced our understanding of the dynamic behaviour of VO_2 and offered up new areas for investigation of ultrafast events in this fascinating substance.

The insulator-metal transition (IMT) in VO_2 's ultrafast dynamics has since been the subject of many studies. The IMT was tracked using ultrafast spectroscopy for various excitation pulse widths [60], and it was discovered that the intrinsic lattice response mostly controlled the onset of the IMT, which happened within a relatively short timescale of about 100 fs. High-resolution spectroscopic reflectivity studies showed that the metallic character caused by photoexcitation did not entirely return to the predicted value of the M1 phase prior to photoexcitation below the structural threshold. The optical response, however, did not entirely match either the M1 or R phase but instead showed a partial recovery on the picosecond timescale. These discoveries further complicate the understanding of the Photoinduced IMT dynamics in VO_2.

Kubler et al.[61] carried out the first time-resolved multi-THz spectroscopy observations, measuring the photo-induced complex conductivity ($\sigma(\omega)$) of a VO_2 sample. They clearly distinguish between two timescales for the IMT response, the first of which lasts for about 60 fs due to the temporary metallization of the film by the photo-excited carriers and the second of which is connected to a $\sim$ 1 ps recovery of the conductivity. At fluences up to around 3 mJ/cm^2, the conductivity recovered completely, and partial recovery continued above a threshold fluence of 4.6 mJ/cm^2. Since these phases were not directly affected by crystal structure, they focused solely on understanding this in terms of the M1 and R phases, and they offered a qualitative description based on the electron relaxation in the R phases.

The IMT was thoroughly examined by Cocker et al.'s THz spectroscopy studies [62], which included a temperature range from 300 K to 17 K. They showed that the fluence threshold strongly depends on temperature and underlined the important roles played by both Mott- and Peierls-like mechanisms. They put up a hypothesis that, in addition to dimer modes, a critical electron density on the V-V dimers causes the transition, confirming the IMT's non-thermal character. Even though there was no clear structural evidence, they saw signs of an intermediate metallic phase that was characterized by intact Peierls distortion and reduced Mott correlations.

In a recent research by Morrison et al. [8], fascinating new information about the photoinduced insulator-to-metal transitions (IMTs) in M1 VO_2 was obtained by a combination of ultrafast electron diffraction and mid-infrared spectroscopy measurements to probe both the structural and electronic aspects of the IMT under identical photoexcitation conditions. Two unique IMTs were seen, one of which was connected to the anticipated lattice-structural transition between M1 and R crystallography predicted by the phase diagram and happening at relatively high pump fluence, resembling the equilibrium IMT. The second IMT, which was accessed at a lower pump fluence, revealed a metastable monoclinic metal phase (M) that did not have an equilibrium analogue but kept the crystallographic symmetry of its equilibrium monoclinic phase. For fluences greater than 3.7 mJ/cm^2, the results of mid-infrared spectroscopy revealed metallic behaviour; yet, electron diffraction experiments at this fluence showed that the crystal structure remained monoclinic. Enhanced scattering amplitude of specific low-index Bragg reflections parallel to the c-axis of the rutile structure was observed in diffraction patterns, suggesting a reorganization of unit cell charge while maintaining the symmetry of the monoclinic structure (atomic coordinates). The complex character of the IMT in M1 VO_2 and its varied expressions under varying pump fluences are revealed by these data. Additionally, These experimental studies stimulated a number of theoretical investigations, notably by the A. Millis group which suggested that the photoexcitaiton of M1 VO_2 leads to a phase-transition in the electronic system alone, yielding a monoclinic metallic phase [63].

More recently, Otto et al.[47] paper offers a thorough examination of the time- and fluence-dependent M1 VO_2 upon photoexcitation. The film like other Mott insulators at pump fluences below $\sim$4 mJ/cm^2, demonstrates a short, impulsive increase in conductivity followed by a complete recovery of the insulating state. A phase transition in the electron system occurs above $\sim$4 mJ/cm^2, stabilizing the metallic characteristics by an orbitally selective charge reorganization, and resulting in the M1 phase. Exclusive M phase formation takes place at fluences between $\sim$4 mJ/cm2 and $\sim$8 mJ/cm^2 and takes up 15% to 2% of the film. The M and R phase fractions increase to $\sim$20 mJ/cm^2, when each phase takes up $\sim$50% of the film, causing a heterogeneous response above this threshold. Due to unfavorable strain, the coexistence of M1 and R phases inside a single crystallite is rare. The M1–M transition is a thermally induced phase change in the electron system by itself, driven by increased electron temperature following femtosecond laser excitation. Non-thermal melting affects the structure and characteristics of materials. The M1 band gap's observed collapse and the metallic phase are consistent with the predictions of an orbital selective transition. The paper also deals with the structural bottleneck brought by the photoinduced IMT, establishing a causal relationship between the onset of metallic transport characteristics and structural phase transitions and the IMT's timescale. Researchers learned more about the intricate behaviour of VO_2 after photoexcitation by combining ultrafast electron diffraction and time-resolved spectroscopy, opening up possible channels for optical control.

4.2 Temperature dependent electron diffraction on UES Instruments

After achieving the desired M1 Phase of VO_2 samples (as covered in Chapter 3) the goal of this experimental investigation was to observe the phase transition temperature of these samples by analyzing the recorded electron diffraction intensity patterns with varying the temperature. We installed a new cryostat system (cold-finger) on our UES apparatus to conduct such temperature-dependent measurements. At temperatures ranging from 300 K to 360 K, diffraction patterns were recorded as part of the experiment. Figure 4.2 represents the VO_2 polycrystalline diffraction images at 300K and 350K, white arrow indicates the appearance of new diffraction rings at 350K, indicating the thermally induced structural phase transition from monoclinic to rutile phase as expected for M1 VO_2, which demonstrates the success of the sample development discussed in Ch. 3. To ensure the collection of high-quality data, each diffraction image was painstakingly taken with an exposure time of 3-minutes. A specialized image processing program called "SCIKIT-UED" [64] was used to efficiently analyze the diffraction patterns. The study and interpretation of electron diffraction patterns are the sole purposes of this program. The UED technique enabled us to understand valuable insights into temperature-dependent structural phase transitions that took place in the polycrystalline VO_2 sample. This experiment produced comprehensive data on the behavior of the VO_2 thin film, representing its structural characteristics and assisting in comprehending response to temperature changes. With our new cold finger cryostat system, we are capable of conducting a thorough analysis of the material's electron diffraction behavior under various thermal settings by careful temperature control, prolonged exposure time, and sophisticated image processing methods.

4.2.1 Diffraction Intensity analysis VO_2

As mentioned above, electron diffraction images were taken in a transmission geometry which was used to generate the experimental results from a polycrystalline VO_2 sample. The intensity was

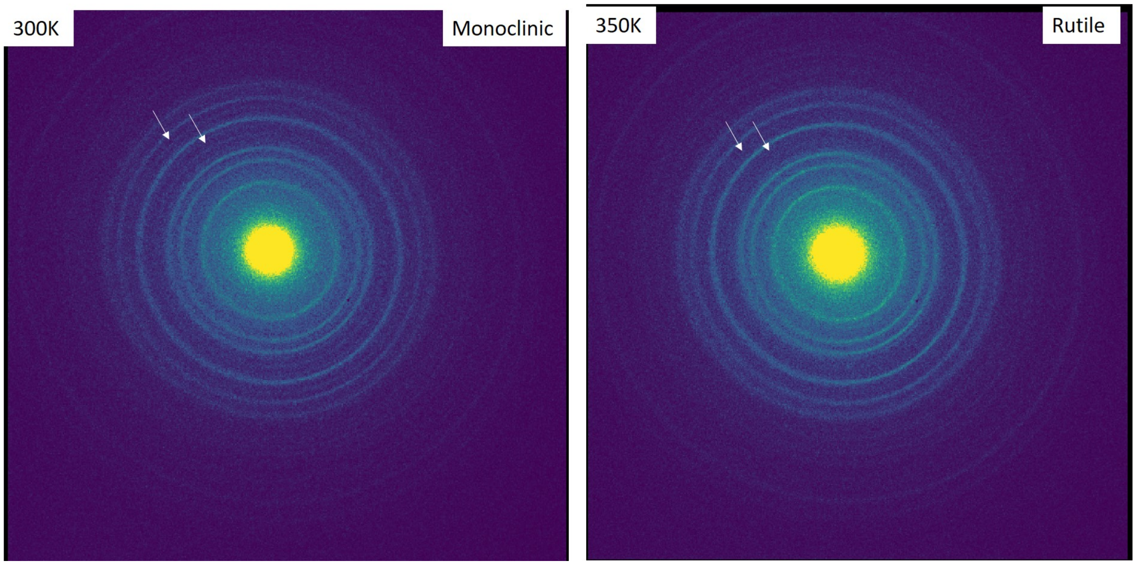

Figure 4.2: Ploycrystalline VO$_2$ UES diffraction patterns at 300K and 350K.

measured from the diffraction images after image background correction and plotted appropriately, as shown in Figure 4.3 . A few weak reflections were found in the ensuing plot, including $(0\bar{1}1)$, (200), $(0\bar{2}1)$, and most notably, $(30\bar{2}\ )$, which is represented by the vertical red line in the image. The peak $(30\bar{2})$'s disappearance is crucial since it is forbidden by the symmetry of the R phase, signifying the successful growth of the PLD thin film technology [47]. Analysis of the figure revealed that this particular peak $(30\bar{2})$, significantly decreases with temperature. This considerable switch in intensity suggests that the polycrystalline VO$_2$ sample underwent a structural phase transition (SPT) that was driven by heat. The change from the monoclinic phase to the Rutile phase and the observed sweep in peak intensity demonstrate how temperature affects the structural characteristics of the material.

The findings from this short experimental work align with previous research on the SPT in VO$_2$ and confirm that the temperature-dependent structural changes observed in the polycrystalline sample are consistent with the predicted behavior of VO$_2$ in the R phase [52]. Since VO$_2$ has the ability to undergo reversible SPT therefore, upon cooling the sample, we see the appearance of $(30\bar{2})$ peak again at 310K (in red), as shown in Figure 4.4.

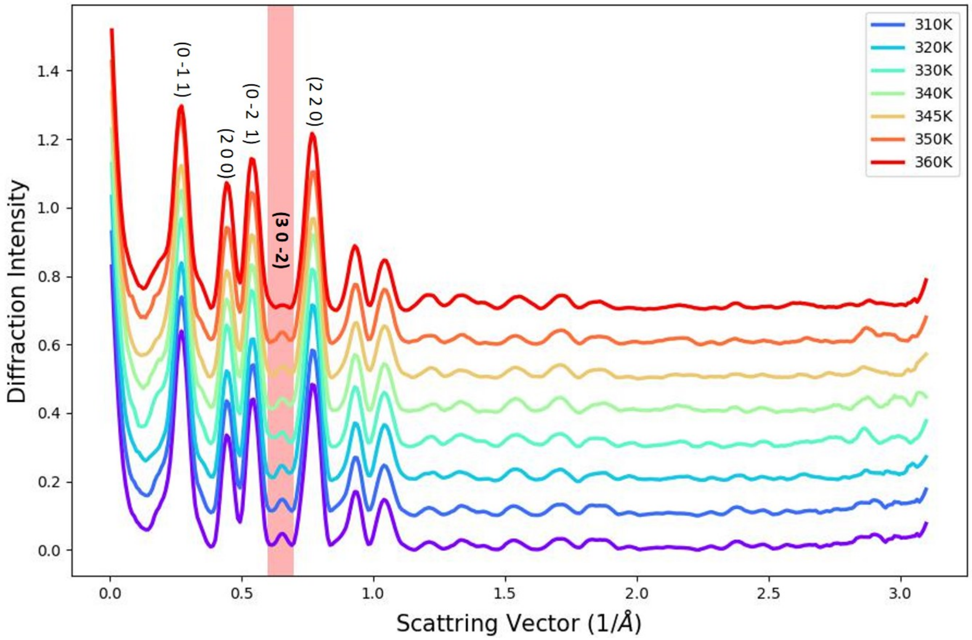

Figure 4.3: Intensity plots of temperature-dependent Electron diffraction while heating up VO_2.

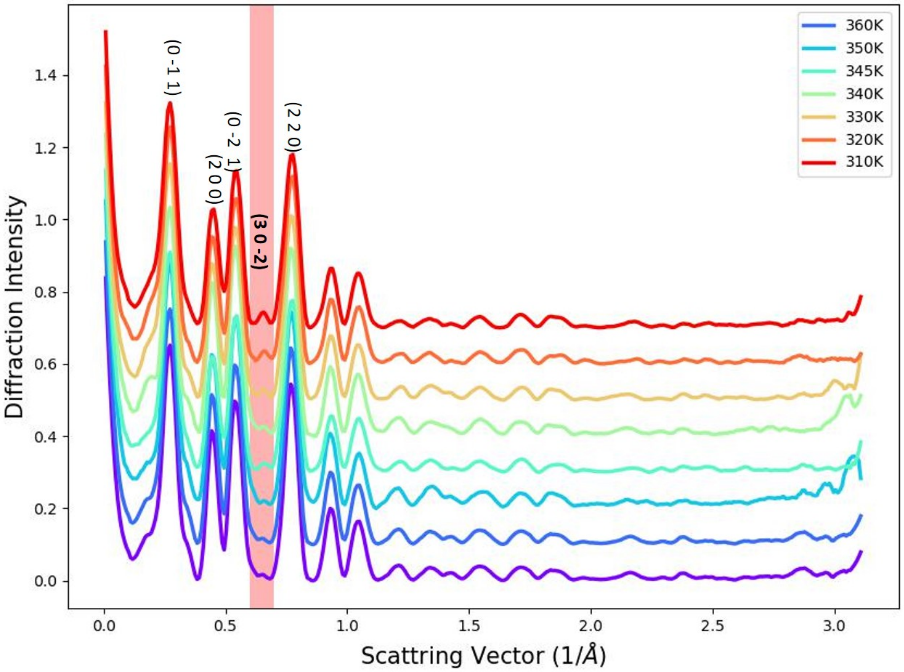

Figure 4.4: Intensity plots of temperature-dependent Electron diffraction while cooling down VO_2.

4.2.2 Hysteresis analysis of VO_2

We plotted the unique behavior of $(30\bar{2})$ peak, which is shown in Figure 4.5 for heating and cooling of VO_2 that provides insight into the phase transition of this fascinating material. The intensity of the $(30\bar{2})$ peaks gradually decreases as the temperature rises during the heating process until a critical temperature is attained. At this critical temperature, a phase transition is seen as a quick, dramatic reduction in peak intensity. The material changes from a low-temperature monoclinic (M) phase to a high-temperature rutile (R) phase during this transition, which is analogous to the insulator-to-metal phase change in VO_2. Similar behavior is seen during the cooling process, although it occurs in the opposite direction. Until it reaches another critical temperature, where another dramatic decrease happens, the peak intensity continuously rises. This cooling-induced transition is equivalent to the metal-to-insulator phase transition, in which VO_2 switches back and forth between the monoclinic (M) phase and the rutile (R) phase. Understanding the material's behavior under various temperature conditions will help you better understand its special properties and potential uses in gadgets and technologies. In the next section, we will explain our future experimentation on determining the mechanism of the photodoped structural phase transition.

4.3 Electron-Phonon Interaction in VO_2 Rutile Phase: Insights and Future Directions:

In previous studies, we have illuminated the (Monoclinic) M1 phase's response to optical excitation, observing a remarkable phase transition within the electronic system. This transition was demonstrated by time-resolved terahertz (tr-THz) spectroscopy and ultrafast electron diffraction (UED), which revealed a change in the electronic structure without a corresponding change in the lattice symmetry [47].

Now a natural question arises, What occurs in the R-phase of VO_2 when exposed to comparable optical excitations? Where does the laser excitation energy goes? Is there a phase transition in the electronic system in the R-phase as has been previously observed in the M1 phase? How long

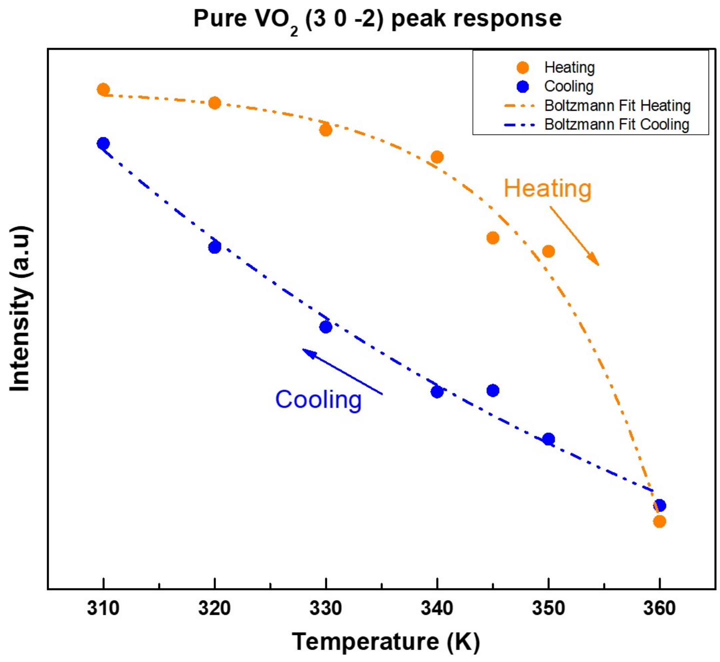

Figure 4.5: $(30\bar{2})$ peak heating (orange circles) followed by cooling (blue circle) to show the expected IMT and hysteresis character of PLD grown VO_2

does it take for electronic excitation to become "heat"; i.e. an increase in lattice vibrations/phonon excitation? This is especially pertinent given the current understanding of the electronic properties of the R-phase. The R-phase of VO_2 is frequently described as a "bad metal" due to its high resistivity. This is due to its "strongly correlated" nature of the electronic system even in the R-phase, which has been suggested by a number of theoretical and experimental investigations [65]. Strongly correlated systems have complex and often non-intuitive electronic properties as the behavior of one electron is greatly influenced by the positions and state of another electron.

Two main limiting cases are possible when a laser excites the R-phase of VO_2 with the questions raised that should be addressed in this experiment:

1. **Change in Electronic Structure without Lattice Change**

2. **Laser Excitation on timescales typical of Electron-Phonon coupling**

4.3.1 Change in Electronic Structure without Lattice Change

Understanding this aspect could be crucial for unraveling the intricate interplay between electronic and lattice degrees of freedom in strongly correlated electron systems like the R-phase of VO_2. We wouldn't anticipate a significant rise in the lattice temperature on the picosecond (ps) timescale if the laser excitation predominantly affects a change in the electronic structure. This could mean little or no Debye-Waller effect. The Debye-Waller effect, known for the attenuation of diffracted electrons beam intensity due to thermal motion of atoms in a crystal, is one significant factor in the reduction of peak intensity. However, if the laser energy is primarily absorbed by the electronic system and induces a change in its structure, the lattice remains relatively unaffected, at least in the immediate aftermath of the excitation.

While the Debye-Waller effect is a primary mechanism for peak attenuation, it is not the sole factor. Other effects, such as inelastic scattering processes, including phonon scattering, electronic excitations, and defect scattering, can also contribute to the reduction of peak intensity in the diffraction pattern. Inelastic scattering results in a loss of energy of the diffracting electrons, which can lead to a broadening and subsequent reduction in the peak intensity. Additionally, structural defects or imperfections in the crystal lattice can lead to diffuse scattering, further reducing the intensity of specific peaks. Therefore, while the Debye-Waller effect is significant, a comprehensive understanding of peak attenuation requires considering these additional scattering phenomena.

4.3.2 Laser excitation on timescales typical of Electron-Phonon coupling

If there is no significant structural change in the electronic system following photoexcitation, the laser energy would primarily manifest as heat. This would result in a significant Debye-Waller effect on the ps timescale, as the lattice temperature would rise due to the energy absorption.

Let's understand it through one published literature in 2016 [5], the article discusses an experimental and theoretical investigation of electron-lattice interactions in a model free-electron metal (aluminum), focusing on the energy transfer from photoexcited electrons to lattice in nonequilibrium states by femtosecond electron diffraction and DFT. Figure 4.6 represents a pump-probe

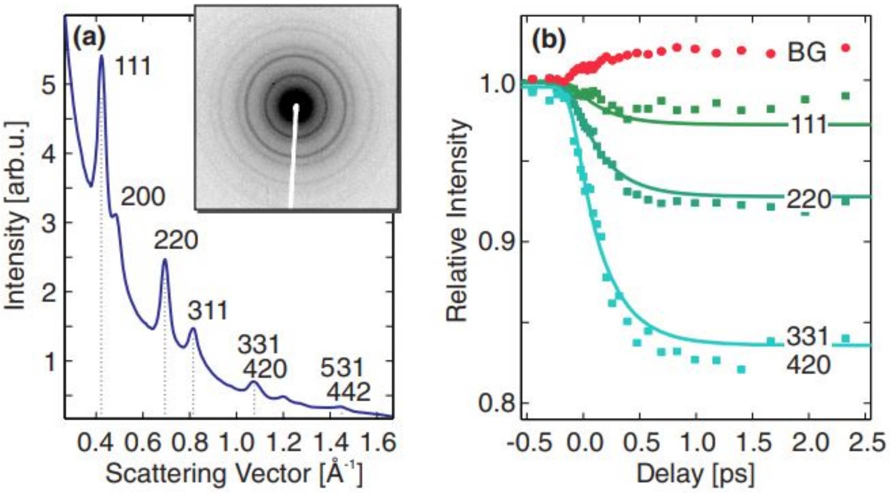

Figure 4.6: (a) An azimuthally integrated and radially average diffraction pattern (inset) of 30 nm thick polycrystalline aluminum, peaks with labels indicating peaks with different orientations. (b) The decrease of the relative intensities of three chosen Bragg peaks and the red scattered line BG (background) of widely scattered electrons is shown in the figure, the other solid lines represent the globe fit [5].

electron diffraction analysis, where 800nm laser was employed for the photoexcitation of 30-nm-thick films composed of freestanding, polycrystalline aluminum at various time delays. Fig. 4.6 (a) shows a diffraction image (inset) of the film and diffracted intensity peaks with labeled peak orientations. Fig. 4.6 (b) shows the intensity of all observed peaks experiences a notable reduction following photoexcitation at time $t = t_0$, ultimately converging to a novel steady-state configuration in under 1 picosecond (ps). Concurrently, within the same temporal domain, a diffusive scattering can also be observed in the background. The observed decrease in intensity can thus be attributed to an energy transfer from excited electrons to the lattice, leading to a higher MSD (Mean Square Displacement) of the atoms.

These results show a significant Debye-Waller effect, it would suggest that the laser energy is primarily being converted into lattice vibrations or phonons, heating up the material. Conversely, if there's a change in the electronic structure without a significant Debye-Waller effect, it would indicate that the laser energy is driving an electronic phase transition, similar to what was observed in the M1 phase previously.

In our experiment, the Debye-Waller effect could arise from directly dumping the heat into the crystal lattice with a pump laser, which leads to an increase in the phonon vibration, always resulting in a peak suppression/attenuation of intensity with time following laser excitation. This suppression in diffraction intensity on a Bragg peak are proportional to the geometric structure factor

$$I \propto |F_0(\mathbf{G})|^2 = \left| \sum_j \exp\left(-M_j(\mathbf{G})\right) f_j(\mathbf{G}) \exp\left(-i\mathbf{G} \cdot \mathbf{r}_j\right) \right|^2 \tag{4.1}$$

where M_j is the Debye-Waller factor, $f_j(\mathbf{G})$ is the atomic form factor and $\mathbf{r}_j$ is the coordinate of atom j in the unit cell. Commonly observed in ultrafast electron diffraction, is the transient suppression of peak intensities due to an increase in $M_j(\mathbf{G})$ known as the transient Debye-Waller effect. The degree to which this is observed and the timescale on which it occurs will go some way to distinguishing between the two limiting cases described above.

4.4 Conclusions

This chapter provides the details of our future experiments and outlook with time-resolved UES measurements on 50 nm thin films grown via PLD on 30nm, 50nm, and 100nm thick Si:N windows. We experimentally confirmed the presence of M1-Phase in these samples. we can track the structural dynamics at the subatomic level following photo-excitation with 800 nm ultrafast laser pulses in UES experiments. When a laser excites the R-phase of VO_2, this excitation may stimulate two distinct processes in the R-Phase of VO_2. One possibility could be a change in electronic structure without lattice change and on the other hand the possibility of the occurrence of the Debye-Waller effect. To grasp the optical control on correlated material like VO_2, UES experiments have provided us with a better experimental understanding, but the work is still far from over.

Bibliography

[1] Daniele Filippetto, Pietro Musumeci, Renkai Li, Bradley John Siwick, Martin Otto, and Martin Centurion Joao Pedro Nunes. Ultrafast electron diffraction: Visualizing dynamic states of matter, june 2022. *Reviews of Modern Physics*, 94(4):045004, 2022.

[2] Valeria Nicolosi, Manish Chhowalla, Mercouri G Kanatzidis, Michael S Strano, and Jonathan N Coleman. Liquid exfoliation of layered materials. *Science*, 340(6139):1226419, 2013.

[3] Yichuan Chen and Mengtao Sun. Two-dimensional ws 2/mos 2 heterostructures: Properties and applications. *Nanoscale*, 13(11):5594–5619, 2021.

[4] Martin Otto. Advancements in electron pulse compression technology applied to ultrafast electron scattering. 2020.

[5] Lutz Waldecker, Roman Bertoni, Ralph Ernstorfer, and Jan Vorberger. Electron-phonon coupling and energy flow in a simple metal beyond the two-temperature approximation. *Physical Review X*, 6(2):021003, 2016.

[6] Marcos Dantus, Mark J Rosker, and Ahmed H Zewail. Real-time femtosecond probing of “transition states”in chemical reactions. *The Journal of Chemical Physics*, 87(4):2395–2397, 1987.

[7] Alvin T Yeh, Charles V Shank, and James K McCusker. Ultrafast electron localization dynamics following photo-induced charge transfer. *Science*, 289(5481):935–938, 2000.

[8] Vance R Morrison, Robert P Chatelain, Kunal L Tiwari, Ali Hendaoui, Andrew Bruhács, Mohamed Chaker, and Bradley J Siwick. A photoinduced metal-like phase of monoclinic vo2 revealed by ultrafast electron diffraction. *Science*, 346(6208):445–448, 2014.

[9] Feng Gai, KC Hasson, J Cooper McDonald, and Philip A Anfinrud. Chemical dynamics in proteins: the photoisomerization of retinal in bacteriorhodopsin. *Science*, 279(5358):1886–1891, 1998.

[10] Amanda L Le Sueur, Rachel E Horness, and Megan C Thielges. Applications of two-dimensional infrared spectroscopy. *Analyst*, 140(13):4336–4349, 2015.

[11] Ronald Ulbricht, Euan Hendry, Jie Shan, Tony F Heinz, and Mischa Bonn. Carrier dynamics in semiconductors studied with time-resolved terahertz spectroscopy. *Reviews of Modern Physics*, 83(2):543, 2011.

[12] Tianlun Yu, Christian E Matt, Federico Bisti, Xiaoqiang Wang, Thorsten Schmitt, Johan Chang, Hiroshi Eisaki, Donglai Feng, and Vladimir N Strocov. The relevance of arpes to high-t c superconductivity in cuprates. *npj Quantum Materials*, 5(1):46, 2020.

[13] Jhih-An Yang, Stephen Parham, Daniel Dessau, and Dmitry Reznik. Novel electron-phonon relaxation pathway in graphite revealed by time-resolved raman scattering and angle-resolved photoemission spectroscopy. *Scientific Reports*, 7(1):40876, 2017.

[14] Robert W Boyd, Alexander L Gaeta, and Enno Giese. Nonlinear optics. In *Springer Handbook of Atomic, Molecular, and Optical Physics*, pages 1097–1110. Springer, 2008.

[15] W Li and DY Li. On the correlation between surface roughness and work function in copper. *The Journal of chemical physics*, 122(6), 2005.

[16] Bradley J Siwick, Jason R Dwyer, Robert E Jordan, and RJ Dwayne Miller. Ultrafast electron optics: Propagation dynamics of femtosecond electron packets. *Journal of Applied Physics*, 92(3):1643–1648, 2002.

[17] Vance R Morrison, Robert P Chatelain, Chris Godbout, and Bradley J Siwick. Direct optical measurements of the evolving spatio-temporal charge density in ultrashort electron pulses. *Optics express*, 21(1):21–29, 2013.

[18] Martin R Otto, LP René de Cotret, Mark J Stern, and Bradley J Siwick. Solving the jitter problem in microwave compressed ultrafast electron diffraction instruments: Robust sub-50 fs cavity-laser phase stabilization. *Structural Dynamics*, 4(5), 2017.

[19] Janis Köster, Baokun Liang, Alexander Storm, and Ute Kaiser. Polymer-assisted tem specimen preparation method for oxidation-sensitive 2d materials. *Nanotechnology*, 32(7):075704, 2020.

[20] Thomas H Kauffmann, Ninel Kokanyan, and Marc D Fontana. Use of stokes and anti-stokes raman scattering for new applications. *Journal of Raman Spectroscopy*, 50(3):418–424, 2019.

[21] Vijay Gopal and Luca Maddalena. Review of filtered rayleigh scattering technique for mixing studies in supersonic air flow. *Progress in Aerospace Sciences*, 120:100679, 2021.

[22] Zhengzong Sun, Zheng Yan, Jun Yao, Elvira Beitler, Yu Zhu, and James M Tour. Growth of graphene from solid carbon sources. *Nature*, 471(7336):124, 2011.

[23] Xisai Zhang, Yang Li, Wenqian Mu, Wenqi Bai, Xiaoxue Sun, Mingyu Zhao, Zhijie Zhang, Fukai Shan, and Zhenyu Yang. Advanced tape-exfoliated method for preparing large-area 2d monolayers: a review. *2D Materials*, 8(3):032002, 2021.

[24] Zhengyang Cai, Bilu Liu, Xiaolong Zou, and Hui-Ming Cheng. Chemical vapor deposition growth and applications of two-dimensional materials and their heterostructures. *Chemical reviews*, 118(13):6091–6133, 2018.

[25] Goki Eda, Hisato Yamaguchi, Damien Voiry, Takeshi Fujita, Mingwei Chen, and Manish Chhowalla. Photoluminescence from chemically exfoliated mos2. *Nano letters*, 11(12):5111–5116, 2011.

[26] Xianlei Li, Xiaopeng Hao, Mingwen Zhao, Yongzhong Wu, Jiaxiang Yang, Yupeng Tian, and Guodong Qian. Exfoliation of hexagonal boron nitride by molten hydroxides. *Advanced Materials*, 25(15):2200–2204, 2013.

[27] Fang Liu, Wenjing Wu, Yusong Bai, Sang Hoon Chae, Qiuyang Li, Jue Wang, James Hone, and X-Y Zhu. Disassembling 2d van der waals crystals into macroscopic monolayers and reassembling into artificial lattices. *Science*, 367(6480):903–906, 2020.

[28] Hualing Zeng, Gui-Bin Liu, Junfeng Dai, Yajun Yan, Bairen Zhu, Ruicong He, Lu Xie, Shijie Xu, Xianhui Chen, Wang Yao, et al. Optical signature of symmetry variations and spin-valley coupling in atomically thin tungsten dichalcogenides. *Scientific reports*, 3(1):1608, 2013.

[29] Robert Schmidt, Gunnar Berghauser, Robert Schneider, Malte Selig, Philipp Tonndorf, Ermin Malic, Andreas Knorr, Steffen Michaelis de Vasconcellos, and Rudolf Bratschitsch. Ultrafast coulomb-induced intervalley coupling in atomically thin ws2. *Nano letters*, 16(5):2945–2950, 2016.

[30] Tristan L Britt, Qiuyang Li, Laurent P Rene de Cotret, Nicholas Olsen, Martin Otto, Syed Ali Hassan, Marios Zacharias, Fabio Caruso, Xiaoyang Zhu, and Bradley J Siwick. Direct view of phonon dynamics in atomically thin mos2. *Nano Letters*, 22(12):4718–4724, 2022.

[31] Ayse Berkdemir, Humberto R Gutiérrez, Andrés R Botello-Méndez, Néstor Perea-López, Ana Laura Elías, Chen-Ing Chia, Bei Wang, Vincent H Crespi, Florentino López-Urías, Jean-Christophe Charlier, et al. Identification of individual and few layers of ws2 using raman spectroscopy. *Scientific reports*, 3(1):1755, 2013.

[32] Mark J Stern, Laurent P René de Cotret, Martin R Otto, Robert P Chatelain, Jean-Philippe Boisvert, Mark Sutton, and Bradley J Siwick. Mapping momentum-dependent electron-phonon coupling and nonequilibrium phonon dynamics with ultrafast electron diffuse scattering. *Physical Review B*, 97(16):165416, 2018.

[33] Samuel Huberman, Ryan A Duncan, Ke Chen, Bai Song, Vazrik Chiloyan, Zhiwei Ding, Alexei A Maznev, Gang Chen, and Keith A Nelson. Observation of second sound in graphite at temperatures above 100 k. *Science*, 364(6438):375–379, 2019.

[34] Zhenhua Ni, Yingying Wang, Ting Yu, and Zexiang Shen. Raman spectroscopy and imaging of graphene. *Nano Research*, 1:273–291, 2008.

[35] Nicola Ferralis. Probing mechanical properties of graphene with raman spectroscopy. *Journal of materials science*, 45:5135–5149, 2010.

[36] Tharith Sriv, Kangwon Kim, and Hyeonsik Cheong. Low-frequency raman spectroscopy of few-layer 2h-sns2. *Scientific reports*, 8(1):10194, 2018.

[37] Wenjie Zhang, Kaiwen Sun, Peng Suo, Xiaona Yan, Xian Lin, Zuanming Jin, and Guohong Ma. Ultrafast photocarrier dynamics in vertically aligned sns2 nanoflakes probing with transient terahertz spectroscopy. *Nanomaterials*, 13(1):5, 2022.

[38] Ying Chen and Man Zhang. Large-area growth of sns 2 nanosheets by chemical vapor deposition for high-performance photodetectors. *RSC advances*, 11(48):29960–29964, 2021.

[39] Ji-Hoon Ahn, Myoung-Jae Lee, Hoseok Heo, Ji Ho Sung, Kyungwook Kim, Hyein Hwang, and Moon-Ho Jo. Deterministic two-dimensional polymorphism growth of hexagonal n-type sns2 and orthorhombic p-type sns crystals. *Nano letters*, 15(6):3703–3708, 2015.

[40] F Giusti, A Marciniak, F Randi, G Sparapassi, F Boschini, H Eisaki, M Greven, A Damascelli, A Avella, and Daniele Fausti. Signatures of enhanced superconducting phase coherence in optimally doped bi 2 sr 2 y 0.08 ca 0.92 cu 2 o 8+ δ driven by midinfrared pulse excitations. *Physical review letters*, 122(6):067002, 2019.

[41] X Wang, LX You, XM Xie, CT Lin, and MH Jiang. Micro-raman study of exfoliated bi2sr2cacu2o8+ δ single crystals with different thicknesses. *Journal of Raman Spectroscopy*, 43(7):949–953, 2012.

[42] LJ Sandilands, JX Shen, GM Chugunov, SYF Zhao, Shimpei Ono, Yoichi Ando, and KS Burch. Stability of exfoliated bi 2 sr 2 dy x ca 1- x cu 2 o 8+ δ studied by raman microscopy. *Physical Review B*, 82(6):064503, 2010.

[43] Petr Shvets, Olga Dikaya, Ksenia Maksimova, and Alexander Goikhman. A review of raman spectroscopy of vanadium oxides. *Journal of Raman spectroscopy*, 50(8):1226–1244, 2019.

[44] Srinivasa Rao Popuri, Alla Artemenko, Rodolphe Decourt, Michaël Josse, UC Chung, Dominique Michau, Mario Maglione, Antoine Villesuzanne, and Michaël Pollet. Structurally restricted phase transitions in vo2 (b) and their impact on transport properties. *The Journal of Physical Chemistry C*, 119(44):25085–25092, 2015.

[45] Nicolas Émond, Badr Torriss, and Mohamed Chaker. Natural and induced growth of vo2 (m) on vo2 (b) ultrathin films. *Scientific Reports*, 8(1):7153, 2018.

[46] Syed Ali Hassan, Shazia Bashir, Khushboo Zehra, and Qazi Salman Ahmed. Structural, morphological and optical properties of pulsed laser deposited znse/znseo3 thin films. *Materials Research Express*, 5(4):046404, 2018.

[47] Martin R Otto, Laurent P René de Cotret, David A Valverde-Chavez, Kunal L Tiwari, Nicolas Émond, Mohamed Chaker, David G Cooke, and Bradley J Siwick. How optical excitation controls the structure and properties of vanadium dioxide. *Proceedings of the National Academy of Sciences*, 116(2):450–455, 2019.

[48] Khaliq Mahmood, Shazia Bashir, M Khaleeq-Ur-Rahman, Nazar Farid, Mahreen Akram, Asma Hayat, and Faizan-Ul-Haq. Effects of substrate temperature on structural, optical and surface morphological properties of pulsed laser deposited zno thin films. *Surface Review and Letters*, 20(03n04):1350032, 2013.

[49] Inyalot Jude Tadeo, Devanshi Bhardwaj, D Sheela, Saluru B Krupanidhi, and Arun M Umarji. Highly photoresponsive vo 2 (m1) thin films synthesized by dc reactive sputtering. *Journal of Materials Science: Materials in Electronics*, 31:4687–4695, 2020.

[50] Jiwei Hou, Zhongping Wang, Zejun Ding, Zengming Zhang, and Jianwu Zhang. Facile synthesize vo2 (m1) nanorods for a low-cost infrared photodetector application. *Solar Energy Materials and Solar Cells*, 176:142–149, 2018.

[51] Jyh Ming Wu and Lian Bang Liou. Room temperature photo-induced phase transitions of vo2 nanodevices. *Journal of Materials Chemistry*, 21(14):5499–5504, 2011.

[52] HF Xu, Y Liu, N Wei, and SW Jin. From vo2 (b) to vo2 (a) nanorods: hydrothermal synthesis, evolution and optical properties in v2o5h2c2o4h2o system. *Optik*, 125(20):6078–6081, 2014.

[53] John B Goodenough. The two components of the crystallographic transition in vo2. *Journal of Solid State Chemistry*, 3(4):490–500, 1971.

[54] AMNF Zylbersztejn and Nevill Francis Mott. Metal-insulator transition in vanadium dioxide. *Physical Review B*, 11(11):4383, 1975.

[55] Volker Eyert. The metal-insulator transitions of vo2: A band theoretical approach. *Annalen der Physik*, 514(9):650–704, 2002.

[56] Silke Biermann, A Poteryaev, AI Lichtenstein, and A Georges. Dynamical singlets and correlation-assisted peierls transition in v o 2. *Physical review letters*, 94(2):026404, 2005.

[57] Cédric Weber, David D O'Regan, Nicholas DM Hine, Mike C Payne, Gabriel Kotliar, and Peter B Littlewood. Vanadium dioxide: A peierls-mott insulator stable against disorder. *Physical review letters*, 108(25):256402, 2012.

[58] WH Brito, MCO Aguiar, K Haule, and G Kotliar. Metal-insulator transition in vo 2: a dft+ dmft perspective. *Physical review letters*, 117(5):056402, 2016.

[59] Michael F Becker, A Bruce Buckman, Rodger M Walser, Thierry Lépine, Patrick Georges, and Alain Brun. Femtosecond laser excitation of the semiconductor-metal phase transition in vo2. *Applied Physics Letters*, 65(12):1507–1509, 1994.

[60] Andrea Cavalleri, Cs Tóth, Craig W Siders, JA Squier, F Ráksi, P Forget, and JC Kieffer. Femtosecond structural dynamics in vo 2 during an ultrafast solid-solid phase transition. *Physical review letters*, 87(23):237401, 2001.

[61] Carl Kübler, Henri Ehrke, Rupert Huber, R Lopez, A Halabica, RF Haglund Jr, and A Leitenstorfer. Coherent structural dynamics and electronic correlations during an ultrafast insulator-to-metal phase transition in vo 2. *Physical Review Letters*, 99(11):116401, 2007.

[62] TL Cocker, LV Titova, S Fourmaux, G Holloway, H-C Bandulet, D Brassard, J-C Kieffer, MA El Khakani, and FA Hegmann. Phase diagram of the ultrafast photoinduced insulator-metal transition in vanadium dioxide. *Physical Review B*, 85(15):155120, 2012.

[63] Zhuoran He and Andrew J Millis. Photoinduced phase transitions in narrow-gap mott insulators: The case of vo 2. *Physical Review B*, 93(11):115126, 2016.

[64] Laurent P René de Cotret and Bradley J Siwick. A general method for baseline-removal in ultrafast electron powder diffraction data using the dual-tree complex wavelet transform. *Structural Dynamics*, 4(4), 2017.

[65] Christopher N Singh, LFJ Piper, Hanjong Paik, Darrell G Schlom, and Wei-Cheng Lee. Correlation-induced emergent charge order in metallic vanadium dioxide. *Physical Review B*, 105(3):035150, 2022.